Department of Micro- and Nanosciences

Analysis of photodarkening effects in ytterbium-doped laser fibers

Joan J. Montiel i Ponsoda

Aalto University

DOCTORAL DISSERTATIONS

Aalto University publication series
DOCTORAL DISSERTATIONS 101/2013

Analysis of photodarkening effects in ytterbium-doped laser fibers

Joan J. Montiel i Ponsoda

A doctoral dissertation completed for the degree of Doctor of Science (Technology) (Doctor of Philosophy) to be defended, with the permission of the Aalto University School of Electrical Engineering, at a public examination held at the large seminar room of the Micronova building (Tietotie 3, Espoo, Finland) on the 7th of June 2013 at 12 noon.

Aalto University
School of Electrical Engineering
Department of Micro- and Nanosciences
Photonics Group

Supervising professors
Prof. Seppo Honkanen
Prof. Harri Lipsanen

Thesis advisor
Dr. Mikko Söderlund

Preliminary examiners
Prof. Risto Myllylä, University of Oulu, Finland
Prof. Shibin Jiang, University of Arizona, USA

Opponent
Prof. Daniel Milanese, Politecnico di Torino, Italy

Aalto University publication series
DOCTORAL DISSERTATIONS 101/2013

ISBN 978-952-60-5216-8 (printed)
ISBN 978-952-60-5217-5 (pdf)
ISSN-L 1799-4934
ISSN 1799-4934 (printed)
ISSN 1799-4942 (pdf)
http://urn.fi/URN:ISBN:978-952-60-5217-5

Unigrafia Oy
Helsinki 2013

Finland

441 697
Printed matter

Author
Joan J. Montiel i Ponsoda

Name of the doctoral dissertation
Analysis of photodarkening effects in ytterbium-doped laser fibers

Publisher School of Electrical Engineering

Unit Department of Micro- and Nanosciences

Series Aalto University publication series DOCTORAL DISSERTATIONS 101/2013

Field of research Photonics

Manuscript submitted 4 February 2013 **Date of the defence** 7 June 2013

Permission to publish granted (date) 14 May 2013 **Language** English

☐ **Monograph** ☒ **Article dissertation (summary + original articles)**

Abstract

Fiber lasers and amplifiers have become very important for many applications, such as telecommunications, materials processing, and medicine. Ytterbium (Yb) doped fibers are the preferred gain media in high peak and average power laser sources. However, the photodarkening effect, which manifests as a time dependent increase of loss in the doped core, is one of the main threats to the efficiency of the Yb-doped gain media leading to degradation of the laser performance.

This thesis focused on developing accurate methods to characterize photodarkening and the associated thermal effects in Yb-doped silica fibers. In a first stage, a method for conducting repeatable photodarkening and thermal bleaching measurements over the same sample was developed. The activation energy associated with the thermal recovery of photodarkening-induced losses was determined. Moreover, thermal cycling studies revealed that a photodarkened sample exhibits a net increase of loss with increasing temperature prior to the initiation of thermal recovery. In addition, the photodarkening-induced absorption spectrum was found to broaden with increasing temperature, resulting in a non-permanent increase of loss in the near-infrared. At the same time, a method to quantify the fiber temperature during the course of photodarkening measurements was established. The fiber temperature was found to correlate with the pump power absorbed by the photodarkening-induced defects. Then, a thermal model was implemented to accurately parameterize the temperature increase of a photodarkened fiber as a function of the pump power. Furthermore, the photodarkening rate was found to follow a power law dependency of 4.5 on the inversion, in case the fiber temperature is properly controlled. Finally, the photodarkening-induced refractive index change, measured by a modal interference method, was found to be positive and in the order of 10^(-5) at around 1080 nm.

Parallel to the experimental work on photodarkening, a new all vapor phase fabrication method was implemented to produce Yb-doped fibers by atomic layer deposition (ALD) in combination with the conventional modified chemical vapor deposition (MCVD) technique. A large mode area Yb-doped aluminosilicate fiber fabricated by this method showed uniform Yb-doping, high lasing efficiency (slope efficiency of 80%) and low background losses. This fabrication method can potentially result in an integrated ALD-MCVD system.

Keywords fiber lasers, rare-earth doped materials, ytterbium, photodarkening, thermal effects

ISBN (printed) 978-952-60-5216-8 **ISBN (pdf)** 978-952-60-5217-5

ISSN-L 1799-4934 **ISSN (printed)** 1799-4934 **ISSN (pdf)** 1799-4942

Location of publisher Espoo **Location of printing** Helsinki **Year** 2013

Pages 157 **urn** http://urn.fi/URN:ISBN:978-952-60-5217-5

Preface

The journey that culminates with this thesis started a few years back, in 2006, at the School of Telecommunications Engineering of Valencia when I was given the opportunity to come to Finland as an exchange student under the Erasmus Programme. The initial plan of returning to Valencia after completing my M.Sc. degree changed when, after being captivated by the Finnish culture and the Nordic summer, I was offered the opportunity to work with the excellent people of the Photonics group.

The work described in this thesis was carried out at the Department of Micro- and Nanosciences in Aalto University (formerly Helsinki University of Technology), during the years 2008-2012. I would like to express my deepest gratitude to Professor Seppo Honkanen, for his supervision, support and encouragement throughout the course of this work. I also want to thank Seppo for his friendship, and for countless hours of talk about football (or soccer as he usually says). I am also grateful to my supervisor Professor Harri Lipsanen, for taking care of me when I first arrived to Micronova in 2007 and for offering me his help in the last stage of my study.

I am specially grateful to Dr. Mikko Söderlund, with whom I have had the privilege to share and enjoy the most interesting findings of this study. I want to thank Mikko for introducing me to the topic of this thesis and for providing me guidance on the research. I am also very thankful to the co-authors of this work, Dr. Changgeng Ye and Dr. Joona Koponen, for their important contribution to this work and helpful discussions, Dr. Ari Tervonen for his valuable advice, comments on the articles and this dissertation, and for providing a good atmosphere of work, and to Dr. Jeff Koplow for his experimental ideas, helpful guidance, and for his help on improving the articles. I am also indebted to Dr. Lars Norin, who has had an important contribution to my last publication, and to Markus Bosund

for carrying out the doping of the soot by ALD.

In addition, I would like to express my gratitude to all my colleagues at the Dep. of Micro- and Nanosciences, especially to Dr. Ya Chen, Lasse Karvonen, Dr. Antti Säynätjoki, Dr. Tapani Alasaarela, Amit Khanna, Aarni Iho, Janne Jaakola, Dr. Steffen Novotny, Henri Jussila, Dr. Sami Kujala, Dr. Marko Mattila, and Pasi Kostamo, for their assistance in experiments, for sharing their knowledge with me, and for providing a great work environment. I acknowledge also Paula Heikkilä for her technical advise.

During these years, I have also had the opportunity to collaborate with the Valencia Nanophotonics Technology Center (NTC) and the *Universitat de València*. Special thanks goes to Dr. Pere Pérez, for enthusiastic discussions in the lab and valuable suggestions, and to Prof. Javier Martí, Prof. Miguel Andrés and Prof. José Luis Cruz for welcoming me in their labs.

Furthermore, I am thankful to José Luis Peralta for his friendship, help, and for tutoring me with LaTeX. Without naming everyone, I would like to thank all my friends for providing me wonderful and relaxing moments during the years.

Finally, the warmest of my gratitude goes to my parents, for their unwavering and unconditional support throughout my studies and in my life that gave me the courage to embark on this journey, to my sister for caring so much about me, and also for trying to improve my English, to my grandparents for their love, to my precious niece Marina, who cheered me up when I needed, and to my dear Rosa for her love, patience and help to this work - You are the best thing that ever happened to me, I love you.

Espoo, May 15, 2013,

Joan J. Montiel i Ponsoda

Contents

Preface i

Contents iii

List of Publications v

Author's Contribution vii

List of Abbreviations ix

List of Symbols xi

1. Introduction 1

2. Rare-earth doped optical fibers 5

2.1 Basics of optical fibers 5

2.2 Rare-earth dopants 7

2.3 Spectral properties of Yb^{3+} 10

2.4 Inversion in Yb-doped fibers 12

2.5 Power scaling 14

2.5.1 Fundamental limitations 15

2.5.2 Large mode area fibers 18

2.5.3 Optimization of the core material 19

3. Fabrication of rare-earth doped fibers 21

3.1 MCVD with solution doping method 23

3.2 Direct nanoparticle deposition (DND) 24

3.3 Current limitations 25

4. Photodarkening in Yb-doped fibers 27

4.1 Inversion dependence 28

4.2 Bleaching 29

4.3 Combined photodarkening and thermal bleaching measurement . . . 30
4.4 Thermal activation energy . . . 33
4.5 Color center formation . . . 35
4.6 Mitigation . . . 37

5. The role of temperature in the photodarkening-induced loss 39
5.1 Post-irradiation heat-induced darkening . . . 40
5.2 Spectral broadening . . . 41
5.3 Photodarkening-induced increase of fiber temperature . . . 44
5.4 Thermal model . . . 45
5.5 Temperature dependence of inversion . . . 47
5.6 Ion dependency discrepancy . . . 49
5.7 Isothermal measurements . . . 51

6. Photodarkening- and thermal bleaching-induced refractive index change 55
6.1 Measurement method . . . 56
6.2 Results . . . 57

7. Fabrication of Yb-doped fibers with atomic layer deposition method 61
7.1 Fabrication process . . . 61
7.2 Doping by atomic layer deposition . . . 62
7.3 Fiber results . . . 64
7.4 Future work . . . 66

8. Summary and outlook 67

Bibliography 71

Publications 83

List of Publications

This thesis consists of an overview and of the following publications which are referred to in the text by their Roman numerals.

I M. J. Söderlund, J. J. Montiel i Ponsoda, J. P. Koplow, and S. Honkanen. Heat-induced darkening and spectral broadening in photodarkened ytterbium-doped fiber under thermal cycling. *Opt. Express*, 17, 12, 9940-9946, June 2009.

II M. J. Söderlund, J. J. Montiel i Ponsoda, J. P. Koplow, and S. Honkanen. Thermal bleaching of photodarkening-induced loss in ytterbium-doped fibers. *Opt. Letters*, 34, 17, 2637-2639, September 2009.

III J. J. Montiel i Ponsoda, M. J. Söderlund, J. P. Koplow, J. J. Koponen, and S. Honkanen. Photodarkening-induced increase of fiber temperature. *Appl. Optics*, 49, 22, 4139-4143, August 2010.

IV J. J. Montiel i Ponsoda, J. P. Koplow, M. J. Söderlund, J. J. Koponen, and S. Honkanen. Analysis of temperature dependence of photodarkening in ytterbium doped fibers. *Opt. Eng.*, 50, 11, 111610-1–111610-9, November 2011.

V C. Ye, J. J. Montiel i Ponsoda, A. Tervonen, and S. Honkanen. Refractive index change in ytterbium-doped fibers induced by photodarkening and thermal bleaching. *Appl. Optics*, 49, 30, 5799-5805, October 2010.

VI J. J. Montiel i Ponsoda, L. Norin, C. Ye, M. Bosund, M. J. Söderlund, A. Tervonen, and S. Honkanen. Ytterbium-doped fibers fabricated with atomic layer deposition method. *Opt. Express*, 20, 22, 25085-25095, October 2012.

Author's Contribution

Publication I: "Heat-induced darkening and spectral broadening in photodarkened ytterbium-doped fiber under thermal cycling"

The author participated in the design of the experiment and in conducting the experiments. The author also participated in the data analysis, and contributed to the preparation of the manuscript.

Publication II: "Thermal bleaching of photodarkening-induced loss in ytterbium-doped fibers"

The author participated in the design of the experiment, participated in conducting the experiments, and contributed to the preparation of the manuscript.

Publication III: "Photodarkening-induced increase of fiber temperature"

The author had a major role in designing the experiment, did the experiments, analyzed the data, and prepared the manuscript.

Publication IV: "Analysis of temperature dependence of photodarkening in ytterbium doped fibers"

The author led the design of the experiment, did the experiments and simulations, and prepared the manuscript.

Publication V: "Refractive index change in ytterbium-doped fibers induced by photodarkening and thermal bleaching"

The author designed part of the experiment, contributed to the experimental work, and participated in the preparation of the manuscript.

Publication VI: "Ytterbium-doped fibers fabricated with atomic layer deposition method"

The author participated in the design of the experiment, did all the experiments apart from the soot-preform doping and material analysis, did most of the data analysis, and prepared the manuscript. The MCVD soot-preforms were prepared in Acreo AB (Sweden).

List of Abbreviations

ALD	atomic layer deposition
ASE	amplified spontaneous emission
CCC	chirally coupled core
CT	charge transfer
CW	continuous wave
DCF	double cladding fiber
DND	direct nanoparticle deposition
EDFA	erbium doped fiber amplifier
EDS	energy dispersive spectrometer
ESR	electron spin resonance
FBG	fiber Bragg grating
FWHM	full width at half maximum
KKR	Kramers-Krönig relations
LCF	leakage channel fiber
LMA	large mode area
MCVD	modified chemical vapor deposition
MMF	multi-mode fiber
NA	numerical aperture
NIR	near infrared
ODC	oxygen deficiency center

OVD	outside vapor deposition
PCF	photonic crystal fiber
RE	rare-earth
SBS	stimulated Brillouin scattering
SMF	single-mode fiber
SPM	self-phase modulation
SRS	stimulated Raman scattering
RIC	refractive index change
RT	room temperature
SEM	scanning electron microscope
SMF	single-mode fiber
UV	ultra violet
VAD	vapor axial deposition

List of Symbols

α_{max}	maximum absorption coefficient change [dB/m]
Γ	overlap factor
$\Delta\alpha$	photodarkening-induced absorption coefficient change [dB/m]
Δn_{PD}	photodarkening induced refractive index change
$\Delta \mathrm{T}_{PD}$	temperature increase associated with photodarkening [°C]
$\Delta \mathrm{T}_{QD}$	temperature increase associated with quantum defect [°C]
λ_0	cross-over wavelength [nm]
σ_a	absorption cross section [m^2]
σ_e	emission cross section [m^2]
τ_{21}	radiative lifetime [s]
$1/\tau$	photodarkening rate parameter [s^{-1}]
Abs_{920nm}	ytterbium absorption at 920 nm wavelength [dB/m]
A_{eff}	effective mode area [m^2]
E_d	demarcation energy [eV]
g_B	Brillouin peak gain coefficient [m/W]
g_R	Raman peak gain coefficient [m/W]
h	convective coefficient [W/m^2·K]
h_p	Planck constant [J·s]
I	incident light intensity [W/m^2]
k	thermal conductivity [W/m·K]

k_B	Boltzmann constant [eV/K]
L_{eff}	effective nonlinear length [m]
N_1	normalized lower state population
N_2	normalized upper state population
Q_0	heat density [W/m^3]
R	pump transition rate
T_c	coolant temperature [K]
v_0	vibrational frequency [s^{-1}]
v_s	signal frequency [s^{-1}]
v_p	pump frequency [s^{-1}]
W	signal transition rate

1. Introduction

Fiber lasers and amplifiers have recently emerged as key devices in many applications, including telecommunications, materials processing and medicine. Fiber amplifiers are used, for example, in long distance optical fiber communications to amplify the signals without the need for expensive optoelectronic regenerators. This capability, enabled by the erbium-doped fiber amplifier (EDFA), has permitted a dramatic increase in the capacity of the telecommunications systems enabling high data rates necessary for today's Internet communication [1]. Recently, the use of fiber amplifiers also in many free space communications networks has been reported, both in terrestrial and satellite-based systems [2]. Fiber lasers with high output power have been extensively employed in materials processing applications. These applications include drilling, marking, cutting and soldering, which play an important role in the automobile, aerospace and building industry [3]. In addition, fiber lasers have also the potential to make a significant impact in the field of medicine due to the intrinsic geometry of the fiber, its compact size and high efficiency. These features are well-suited for endoscopic and surgical procedures [4] such as tracking tumors [5], and for other ablative procedures beneficial for treating kidneys, brain, skin and larynx [6].

The idea for a fiber laser was proposed in 1961 by Elias Snitzer [7, 8], soon after the first detailed proposal of building a laser (at that time called "optical maser") by Schawlow and Townes in 1958 [9] and the first demonstration of a laser by Maiman in 1960 [10]. Snitzer's first experimental demonstration used a barium crown glass fiber doped with trivalent neodymium ions [8]. A few years later (1964), Snitzer and Koester demonstrated the first fiber optic laser amplifier [11]. This fiber amplifier consisted of a neodymium-doped fiber and flash lamps for inducing excitation of the Nd^{3+}-ions (i.e. pumping). However, progress was slow

until mid 1980's when the chemical vapor deposition process used to produce low loss fibers [12] was modified to incorporate doping of rare-earth (RE) ions [13–15]. Soon thereafter, research groups at the University of Southampton and AT&T Bell Laboratories developed in parallel the first EDFAs [16, 17]. The ability of the EDFAs to provide gain at the third telecommunication window attracted much interest and resources from the telecommunications industry, which boosted the development of the fiber laser and amplifier technology. Since then, fiber lasers and amplifiers have shown rapid progress in terms of power scalability [18] and operating wavelength regimes [19–22].

The maximum output power of fiber lasers in continuous wave (CW) operation has grown exponentially over the last decade [18], reaching a record power of 10 kW in the single-mode regime in 2010 [23]. The high output power and other excellent properties offered by the fiber lasers, both CW and pulsed ones, make them highly attractive for a variety of applications. The intrinsic geometry of the optical fiber offers excellent thermo-optical properties, owing to the high surface area to volume ratio, resulting in excellent heat dissipation and distribution of the thermal load over a long length [24]. In addition, optical fibers are excellent in achieving diffraction-limited beam quality (single-mode fibers), high gain and power independent mode distortions [25]. Furthermore, advances in the development of passive components such as fiber Bragg gratings (FBG) and pump-combiners, allows for all-fiber laser systems, making them alignment-free, compact and robust.

Ytterbium (Yb) doped fibers are the preferred gain media for building high power laser systems. Yb-doped fibers benefit from having a broad absorption band at the infrared wavelength region, where high power pump diodes are available. In addition, the practical absorption wavelengths are close to the emission wavelength, resulting in a high energy efficiency, and thus low thermal load. However, high power Yb-doped fiber laser systems suffer from some detrimental effects that reduce the reliability of these laser sources [25]. The photodarkening effect is one of the main threats to the efficiency of the Yb-doped gain media and manifests as a time dependent increase of a background loss in the doped core. Although this effect was already observed in 1997 [26], its importance was not recognized and it was not studied until 2005 when the first scientific paper on photodarkening was published [27]. Since then, progress has been made in understanding this effect and in reducing its impact, mainly through

optimization of the core glass composition. However, a detailed description of the process driving the induced loss and methods to mitigate it without important trade-offs are still under study.

The aim of this work has been to improve the understanding of the photodarkening effect in Yb-doped silica fibers through the implementation of accurate and repeatable characterization methods. Particular goals of the study have been to investigate the influence of temperature on the photodarkening process and to understand the thermodynamic properties of the photodarkening-induced defects. In addition, a new all-vapor phase fabrication method for producing Yb-doped fibers has been implemented aiming to improve the homogeneity of the core material and thus, enhancing the laser efficiency through reduction of clustering, and therefore photodarkening.

The thesis is organized as follows. Chapter 2 introduces some basic and fundamental properties of the rare-earth doped fibers and typical methods used for power scaling. Its fundamental limitations are also discussed. Chapter 3 reviews the fabrication of rare-earth doped fibers and describes the state-of-the-art fabrication techniques. In addition, current limitations of these fabrication methods are discussed. Chapter 4 reviews the photodarkening effect in Yb-doped fibers, describes the implemented measurement method and presents a study of a thermal bleaching process. Chapter 5 focuses on studying the temperature influence on the photodarkening process and characterizing the photodarkening-induced fiber temperature change during irradiation. An isothermal method for controlling the fiber core temperature is also presented. Chapter 6 presents a measurement approach for determining the refractive-index change induced by photodarkening. In Chapter 7 a new fabrication method of producing Yb-doped fibers by the atomic layer deposition (ALD) in combination with the conventional modified chemical vapor deposition (MCVD) technique is presented. Finally, in Chapter 8, a summary is presented and future research directions are briefly discussed.

2. Rare-earth doped optical fibers

2.1 Basics of optical fibers

A typical optical fiber is a cylindrical structure made of glass that is composed by a core layer of diameter a and a refractive index n_1, and a surrounding cladding layer of diameter b and a refractive index n_2. See Fig. 2.1. To allow light confinement in the core, n_2 is slightly lower than n_1. The structure also contains a third layer surrounding the cladding, which is typically a polymer coating with a refractive index n_3 higher than n_2. The main purpose of the polymer coating is to maximize the fiber strength and to protect the inner layers against microbending.

In a double cladding fiber (DCF), the refractive index n_3 of the polymer coating is lower than n_2, allowing the confinement of light also in the inner cladding [28]. In some cases, the third layer is also made of silica glass, which is doped with fluorine or boron to lower the refractive index of silica. This structure is referred to as an all-glass fiber, although the outer cladding is usually also coated with a polymer for mechanical durability.

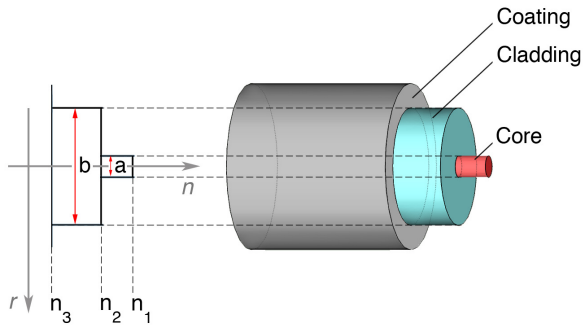

Figure 2.1: Schematic of a double cladding optical fiber and its transverse refractive index profile.

The core refractive index n_1 and the cladding refractive index n_2 determine the maximum angle at which an incident ray can be coupled in the fiber core. The sine of this maximum acceptance angle is the numerical aperture (NA), and it can be calculated from the index difference:

$$NA_{core} = \sqrt{n_1^2 - n_2^2}. \tag{2.1}$$

The NA of a single-mode fiber (SMF) has a value typically in the range of 0.10 to 0.14, while the NA of a multi-mode fiber (MMF) is about 0.3. In a DCF with a fluoroacrylate polymer as the outer layer the light is coupled in the inner cladding with an NA that can be as high as 0.45. On the other hand, in all-glass fibers the acceptance angle is smaller, the NA is typically less than 0.22.

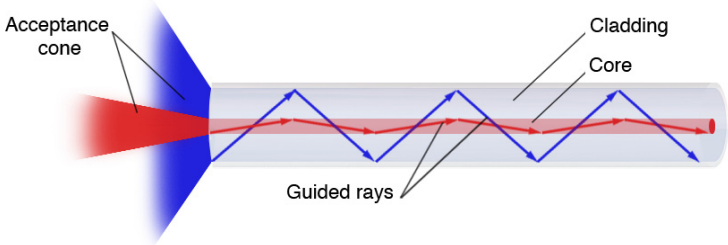

Figure 2.2: Schematic diagram of a double cladding fiber with acceptance cone.

Unlike in single cladding fibers, in DCFs the pump power is launched in the inner cladding. The larger cross section of the inner cladding and the higher NA enable a much simpler and more efficient launch of pump light and the use of high power laser diodes with less demanding beam quality. The cladding cross section is typically non-round as shown in Fig. 2.3, which eliminates the propagation of rays with no overlap with the doped core and thus increases the efficiency of the pump absorption.

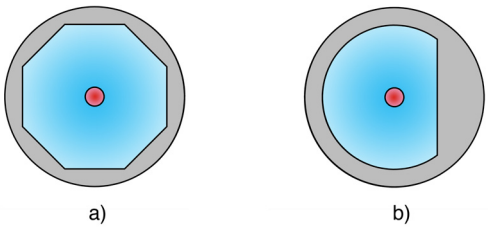

Figure 2.3: Cross sections of two double cladding fibers: (a) Octagonal shape, (b) D-shape.

The number of modes supported by the fiber is determined by the normalized frequency or V-number [29]:

$$V = \frac{2\pi a NA}{\lambda}, \tag{2.2}$$

where a is the core radius and λ is the wavelength of the propagating light in vacuum. A SMF satisfies the condition that V <2.405, meaning that at higher values of V the fiber becomes multi-moded. The core radius of a SMF is usually in the range of 3 to 5 μm, depending on the operating wavelength. In MMFs the core radius is much higher, typically from 25 to 30 μm. The standard dimension for the inner cladding radius is 62.5 μm, which is large enough to confine the fiber core propagating modes entirely, both for single- and multi-mode fibers.

A way to couple the pump power into the inner cladding of a DCF is to inject the multi-mode pump light from the side with the proper NA and beam size, as shown in Fig. 2.2. This pump scheme, known as end-pumping, has the advantage that it is easy to implement, but it limits the access points of the fiber to only two. In addition to that, the thermal load from uncoupled pump needs to be removed, which is generally a major issue in high power lasers. Efficient pump coupling can be achieved using a pump combiner. In this passive component, multiple fibers are thermally tapered and fused to a single output fiber so that the light from multiple inputs can be couple to the inner cladding of a single DCF [30].

2.2 Rare-earth dopants

Fiber lasers and fiber amplifiers are based on optical fibers doped with rare-earth (RE) ions. The RE ions group is mainly composed of lanthanides, which are 15 chemical elements of the periodic table with an atomic number ranging from 57 to 71. The ions of the most interest are neodymium (Nd^{3+}), erbium (Er^{3+}), ytterbium (Yb^{3+}) and thulium (Tm^{3+}), which are incorporated into the fiber core as oxides. In a trivalent state, optical absorption and emission causes transitions between the energy states within an inner shell (4f), while the outer shells (5d and 5p) remain intact and prevent perturbations by external fields. In a pump process an RE-ion in an initial ground state can absorb the energy of an incoming pump photon of energy $E_1 = h_p v_1$ reaching a higher energy level E_h (see Fig. 2.4(a)), where h_p is the Planck constant, and v_1 is the frequency of the in-

coming photon. When the ion is in the excited state it can rapidly relax to a somewhat lower energy level E_m through a non-radiative de-excitation process that involves the creation of a phonon, i.e. a quantized vibration of the surrounding medium. From this level, de-excitation to the ground state can take place either by spontaneous or stimulated emission, and in both cases a photon of energy $E_3 = E_m - E_g$ is emitted.

In stimulated emission an incoming photon with energy E_3 promotes de-excitation of the ion from the upper lasing level E_m, with the creation of a photon having the same properties of phase, polarization and direction as the incoming photon, and thus leading to amplification of light. On the other hand, if the ion is spontaneously de-excited, the photon is emitted with random phase and direction. In an amplification process the number of stimulated emissions exceeds by far the spontaneous emissions. When the ion is relaxed directly to the ground state the process follows a three level lasing scheme, which takes place, e.g. in Yb-doped fibers when pumped at 920 nm or 976 nm with lasing at longer wavelengths. There exists the possibility that the ion is de-excited to another level, from which it relaxes non-radiatively to the ground state completing a four level lasing process. Fig. 2 shows the schemes of the three and four level lasing processes. The lasing process can follow a different scheme depending on the RE-ion and the pump wavelength of choice, but usually it can be simplified to either a three or a four level laser scheme [1].

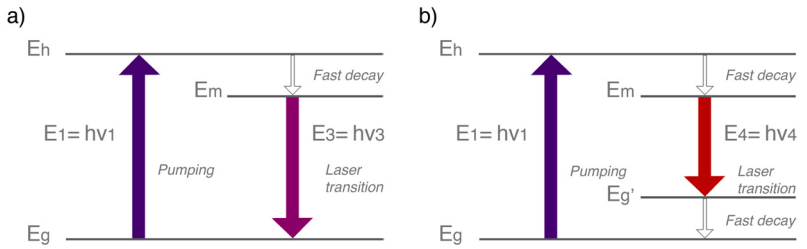

Figure 2.4: Energy level diagrams: (a) Three-level lasing scheme (b) Four-level lasing scheme.

In a three level scheme, absorption from the ground state to the upper lasing level with energy E_m can occur, provoking reabsorption of emitted photons. As a consequence, in order to achieve gain, higher levels of pump power are required. This is not the case in lasers following a four level laser scheme, which benefit from having lower values of threshold powers making them more suitable for many applications.

The wavelengths of pump absorption and signal emission depend on the

energy level arrangement of the ions in the host glass. Table 2.1 summarizes the main laser active RE-ions with their common host glasses and emission wavelengths appearing in an order of importance.

Neodymium was the first of the RE-ions that was used in a fiber laser [8] and in a single-mode fiber laser [31], and it still remains as one of the most used doping elements [32, 33]. Additionally, the first double cladding fiber laser used Nd^{3+} as the doping material [28]. Stimulated emission is obtained at different wavelengths within three fluorescence bands centered at 0.9, 1.06, and 1.35 μm, while inversion can be achieved by pumping at 0.8 and 0.9 μm. The strongest emission band of Nd^{3+} is the one at 1.06 μm, and with conventional 0.8 μm pumping it corresponds to a true four-level laser scheme. However, in terms of energy the efficiency of Nd^{3+} is low, and as a consequence it has been replaced by Yb^{3+} as the dopant of choice for high-power fiber lasers.

Table 2.1: Rare-earth ions with common host glasses and important emission wavelengths.

Ion	Common host glasses	Important emission wavelengths (μm)
Neodymium (Nd^{3+})	Silicate and phosphate glasses	1.03–1.1, 0.9–0.95, 1.32–1.35
Ytterbium (Yb^{3+})	Silicate glass	1.0–1.1
Erbium (Er^{3+})	Silicate, phosphate and fluoride glasses	1.5–1.6, 2.7, 0.55
Thulium (Tm^{3+})	Silicate, germanate and fluoride glasses	1.7–2.1, 1.45–1.53, 0.48, 0.8
Praseodymium (Pr^{3+})	Silicate and fluoride glasses	1.3, 0.635, 0.6, 0.52, 0.49
Holmium (Ho^{3+})	Silicate and fluorozirconate glasses	2.1, 2.9

Erbium-doped fibers are the most important fibers for applications in telecommunications due to their ability to amplify at about 1.55 μm, which corresponds to the low-loss window of silica fibers. Initially, at the invention of the erbium-doped fiber amplifier (EDFA), the pump source used was centered at visible wavelengths (e.g. at 514 nm) due to the lack of more suitable pumps at longer wavelengths [16, 17]. The development of diode lasers first at 1480 nm and later at 980 nm allowed for a more efficient energy conversion and lower amplification noise [34, 35]. High-power fiber sources are difficult to achieve with Er^{3+} mainly due to three

reasons. First, an erbium-doped fiber pumped at 980 nm has a low energy efficiency due to the large energy difference between pump and signal photons. Second, the absorption bands of the Er^{3+} are relatively weak for 980 and 1480 nm. Third, the Er^{3+} concentration level is strongly limited by ion-to-ion interaction effects that degrade the fiber efficiency [1]. The reduced pump absorption of Er-doped fibers can be partly overcome by co-doping with Yb^{3+} [36]. The ytterbium ions can efficiently absorb pump radiation, and then transfer the energy to a closely located Er^{3+} in the ground state, promoting excitation to the upper lasing level.

Ytterbium has become a very important RE-ion for high-power applications due to its high pump-to-signal energy-conversion efficiency around 1 μm and a very simple electronic structure with only one upper lasing level. A detailed analysis of the spectral properties of Yb^{3+} in silica fibers is presented in section 2.3.

The growing interest in developing high power fiber sources emitting around 2 μm has recently spurred the progress in optical fibers doped with Tm^{3+}. Tm^{3+} has an absorption peak centered at 790 nm, which makes it especially suitable for diode pumping and allows efficient excitation of two Tm ions with a single pump photon, through a cross-relaxation process. By this approach, high power silica based fiber lasers with an output power in excess of 1 kW have been demonstrated [22, 37].

2.3 Spectral properties of Yb^{3+}

Compared to other RE-ions, the energy level diagram of Yb^{3+} ions has a simple structure consisting of two well-separated levels or manifolds: the ground state $^2F_{7/2}$ and the excited state $^2F_{5/2}$. Further splitting of these two manifolds into several sublevels (Stark levels) takes place due to the permanent electric field generated by the charge distribution in the host glass [38]. Figure 2.5(a) depicts the energy level diagram of Yb^{3+} ions within the optical spectral range from visible to the NIR [39]. The upper manifold $^2F_{5/2}$ and the lower manifold $^2F_{7/2}$ have three and four Stark sublevels, respectively (labeled with letters). Because of the Stark splitting, laser transitions can take place between different combinations of sublevels in the two manifolds. The corresponding transitions between the sublevels are not discrete energy levels because of homogeneous and inhomogeneous broadening in the glass at room temperature [40]. Therefore, the pump and lasing wavelengths can be selected (or spontaneously

occur in the case of spontaneous emission) from a broad range of wavelengths as indicated in Fig. 2.5(a).

The cross sections represent the probability that an optically induced transition takes place, corresponding to the absorption or the stimulated emission of light. Thus, the amounts of absorbed and emitted light power at a given frequency can be defined as

$$P_{a,e} = \sigma_{a,e} I, \tag{2.3}$$

where the absorption and emission cross sections are σ_a and σ_e (in units of m^2), respectively, and I is the incident light intensity (in units of W/m^2). Figure 2.5(b) shows the absorption and emission cross sections of Yb^{3+} in aluminosilicate glass. The strong absorption and emission peaks at 975 nm correspond to the transition between levels a and e (a↔e). Those levels are the most thermally populated sublevels according to the Boltzmann's distribution, and thus, represent the most probable transition [40, 41].

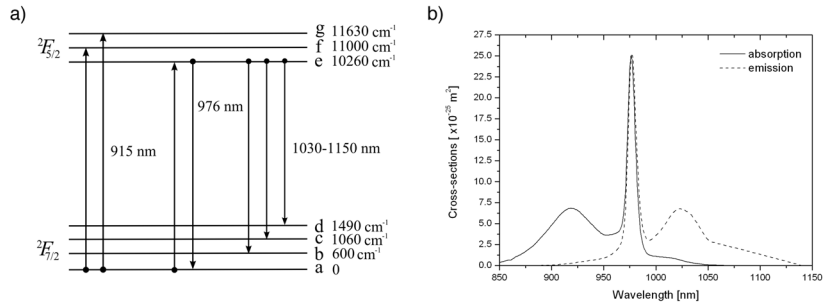

Figure 2.5: (a) Energy level diagram illustrating the ytterbium ground $^2F_{7/2}$ and excited $^2F_{5/2}$ state manifolds and possible transitions between the sub-levels, and (b) absorption and emission cross sections of ytterbium in aluminosilicate glass.

For cladding pumped fibers, pump signal at 975 nm is preferred due to the high pump absorption of Yb-doped fibers at this wavelength. However, pump wavelengths around 915 nm (a→f) are also used to provide more tolerance to the pump diode wavelength, given the broader absorption cross section peak. Moreover, for the pump wavelength at 915 nm, higher inversion can be achieved due to the low value of the emission cross section. On the other hand, gain can be attained at the 975 nm emission peak or over a range of wavelengths at the broader secondary peak centered at ∼1030 nm. Consequently, gain can only be realized at wavelengths longer than

the pump wavelength. Moreover, absorption and emission cross sections are dependent on the host glass and the magnitude of the deviations from one host to another was observed to be up to about 30% [41].

2.4 Inversion in Yb-doped fibers

The term inversion and population inversion are used indistinctly in this dissertation to refer to the fraction of ions in the excited state over the total RE-ion density. Inversion in Yb-doped fibers can be analyzed by considering a three level laser system (see Fig. 2.4(a)). The level 1 is the ground state, with a normalized population of ions N_1. The level 2 is the metastable level or the lasing level, with a normalized population of ions N_2, and the level 3 is the pump level. For Yb^{3+} ions, the pump level is a degenerate level (Stark sublevel) within the level 2. Since the thermalization of the sublevel populations is very fast and the transition from the pump level (level 3) to the metastable level (level 2) is non-radiative, the system can be reduced to a two-level laser system [41]. This approximation was demonstrated to be valid also for fibers doped with Er^{3+} [42].

The rate equations corresponding to the upper (N_2) and lower (N_1) state populations are:

$$\frac{dN_2}{dt} = (R_{12} + W_{12})\, N_1 - (R_{21} + W_{21} + A_{21})\, N_2, \tag{2.4}$$

$$\frac{dN_1}{dt} = -(R_{12} + W_{12})\, N_1 + (R_{21} + W_{21} + A_{21})\, N_2, \tag{2.5}$$

where R is the pump transition rate, W is the signal transition rate and A is the spontaneous emission transition rate coefficient. In steady-state, the populations are time-invariant, i.e. dN_i/dt=0 (i=1,2), and therefore these equations can be reduced to

$$N_2 = \frac{R_{12} + W_{12}}{R_{12} + R_{21} + W_{12} + W_{21} + A_{21}}, \text{ and} \tag{2.6}$$

$$N_1 = 1 - N_2. \tag{2.7}$$

The transition rates are

$$R_{12,21} = \sigma_{a,e}(v_p)\frac{I_p}{h_p v_p}, \tag{2.8}$$

$$W_{12,21} = \sigma_{a,e}(v_s)\frac{I_s}{h_p v_s}, \text{ and} \tag{2.9}$$

$$A_{21} = \frac{1}{\tau_{21}}, \tag{2.10}$$

where σ_a and σ_e are the effective absorption and emission cross sections, and v_p and v_s are the pump and signal frequencies. I_p and I_s are the pump and signal intensities (in units of W/m^2), h_p is the Planck constant, and τ_{21} is the radiative lifetime of the excited state. The upper-state lifetime is defined as the time after which the upper-level population has decayed to $1/e$ in absence of pumping and stimulated emission [1]. In particular, radiative lifetime takes into account only the decay caused by spontaneous emission. Values for the radiative lifetime of around 0.8 ms are typically measured, although it may vary by about 30% between fibers with different host glass [41].

In this dissertation, cladding pumping is used to achieve controllable and uniform inversion in Yb-doped fibers. For a double cladding fiber, the pump intensity I_p can be calculated by dividing the pump power (in W) with the cladding area [43]. The fiber samples used are short in length, typically $<$2 cm, and consequently, the amplified spontaneous emission (ASE) can be neglected ($W_{12,21}$=0) [44]. Moreover, no signal in the Yb amplification region is launched. Under these conditions, the normalized inversion is well approximated using the relations

$$N_2 = \frac{\sigma_a(v_p)}{\sigma_a(v_p) + \sigma_e(v_p)} \frac{1}{1 + I_{sat}/I_p}, \text{ and} \tag{2.11}$$

$$I_{sat} = \frac{h_p v_p}{(\sigma_a(v_p) + \sigma_e(v_p))\,\tau_{21}}, \tag{2.12}$$

which were derived from the equations (2.6)-(2.10). This shows that the inversion can be controlled by tuning only one parameter, i.e. the pump power. With strong cladding pumping at 915 nm, inversion levels well above 90% can be reached, while a strong pump at 975 nm creates a maximum of 50% inversion. This is due to the fact that at the 975 nm wavelength Yb-absorption and -emission cross sections are equal [41]. A detailed study on inversion distributions in short Yb-doped fibers with different pumping configurations was published by Koponen et al. [44].

Furthermore, in Publications IV, V and VI inversion in the fiber was in some cases estimated by simulation using a commercial software (Liekki Application Designer). This simulation tool uses a full numerical spatial-mode modeling, and thus, it is expected to give a better estimation of the inversion as described above [45].

2.5 Power scaling

During the past decade, high power fiber lasers and amplifiers have experienced a tremendous progress in power scaling, reaching continuous wave (CW) output power levels beyond 3 kW with near diffraction-limited beam quality [46]. This increase in the output powers has mainly occurred due to the advances in the fabrication and design of RE-doped fibers with a double cladding structure, the excellent thermo-optical properties of optical fibers, and the development of high power pump diode sources [25]. Optical fibers doped with Yb are particularly interesting due to their high optical-to-optical energy efficiency, well above 80% [19]. This excellent energy efficiency is mainly explained by the low energy difference between the pump and signal photon, i.e. the quantum defect that can be expressed as

$$q = h_p v_p - h_p v_s = h_p v_p \left(1 - \frac{\lambda_p}{\lambda_s}\right), \tag{2.13}$$

where h_p=6.626·10^{-34} Js is the Planck constant, and v_p and v_s are the pump and signal frequencies, respectively. The quantum defect is often expressed as a fraction of the absorbed pump photon energy, the term in parenthesis, which dissipates as heat. Yb-doped fibers have typically a quantum defect of less than 10%, which results in a low thermal load. In addition to that, the simple energy structure of Yb allows for very high dopant concentrations before the onset of concentration quenching processes that would limit the laser efficiency [41].

Currently, the reported maximum available CW output power from an Yb-doped fiber laser in the single-mode regime is as high as 10 kW [23]. This fiber laser uses an advanced method of pumping, named tandem-pumping, in which one or several fiber lasers pump another one [25]. This approach is mainly used to enable pumping close to the emission wavelength so that the quantum defect is low and thereby also the thermal load. The 10 kW fiber laser was pumped by an Yb-doped fiber pump lasers at 1018 nm and emitted at 1070 nm, resulting in a quantum defect of less than 5%.

Although the highest values of output powers have been achieved for Yb-doped fibers, there is also interest in increasing the power of laser sources working at longer wavelengths that are used in applications such as free-space communications and light-imaging detection. At the 1.5-1.6 μm wavelength range, the highest power levels have been demonstrated for systems based on cladding-pumped Er/Yb co-doped fibers. By using this

approach, a record power level of 300 W of CW signal at 1567 nm has been demonstrated by Jeong et al. [21]. However, the laser efficiency of this type of lasers is reduced at high output powers due to strong co-lasing at 1067 nm resulting from the emission of Yb ions. Tremendous success in achieving power scaling also at 2.05 μm has been demonstrated by large mode area (LMA) Tm-doped silica fibers showing >1 kW of output power and a slope efficiency of roughly 53% [22].

2.5.1 Fundamental limitations

The two main limitations to the power scalability of fiber lasers are nonlinear effects and thermal management. The nonlinear effects are related to the properties of the optical fiber itself, which entails laser radiation with a small effective mode area and long propagation length. This spurs the onset of nonlinear effects such as stimulated Raman scattering (SRS), stimulated Brillouin scattering (SBS) and self-phase modulation (SPM), although the latter effect can be neglected for CW fiber lasers [29]. The SRS causes molecular vibrations that result in the frequency downshift (by $\sim$13 THz) for a fraction of the propagating signal and the emission of phonons. The large wavelength shift of the created signal, i.e. greater than 60 nm for an Yb-doped fiber laser emitting around 1 μm, is unacceptable for most applications. The SBS creates also a signal with frequency downshift that propagates in the backward direction with respect to the incident beam (and phonons). The frequency shift is in this case relatively small, about 15 GHz in Yb-doped fibers operated at around 1060 nm. The threshold power for SRS is approximated by [29]

$$P_{th}^{SRS} \cong \frac{16 A_{eff}}{g_R L_{eff}}, \tag{2.14}$$

where A_{eff} is the effective mode area of the propagating mode, g_R the Raman peak gain coefficient (10^{-13} m/W for silica at 1 μm wavelength), and L_{eff} the effective nonlinear length. Similar expression can be derived for the SBS:

$$P_{th}^{SBS} \cong \frac{21 A_{eff}}{g_B L_{eff}}, \tag{2.15}$$

where g_B is the Brillouin peak gain coefficient, which is almost independent of wavelength ($5{\cdot}10^{-11}$ m/W for silica fibers). These two nonlinear effects manifest as a loss mechanism. The threshold of SBS is relatively low in optical fibers and thereby introduces the strongest limitation to the power scaling of single-frequency fiber lasers. It is therefore possible to

raise the Brillouin threshold by increasing the spectral bandwidth of the signal. It is estimated that at a spectral bandwidth above approximately 0.5 GHz, the power scaling would be restricted by SRS. The effect of SBS can be also suppressed by reducing the fiber length or longitudinally varying the fiber temperature [47]. On the other hand, the mitigation of the SRS is only possible through the reduction of the fiber length or signal power, or by means of specialty fiber designs [48–50].

The heat generation due to the quantum defect can damage an optical fiber through coating degradation, fracture or even melting of the core [24]. In Yb-doped fibers, the fraction of the pump power that is absorbed and converted into heat is approximately 15%. This means a heat generation of more than 150 W per kilowatt of output power. Therefore, special attention should be given to cooling of the fiber in order to maintain efficiency and avoid damage [43, 51].

Brown and Hoffmann have implemented a 2-dimensional model to simulate the radial temperature distribution of bare double cladding fibers [24]. The model assumes the heat load generated by the quantum defect of Yb is distributed uniformly in the core (with no variation along the fiber), and that the core and the cladding regions have the same thermal and mechanical properties. Figure 2.6(a) shows the geometry of the modeled fiber. The steady-state heat equation for an isotropic medium (considering two regions with cylindrical symmetry) can be expressed as [24]

$$\frac{1}{r}\frac{\partial}{\partial r}\left(r\frac{\partial T_{core}(r)}{\partial r}\right) = -\frac{Q_0}{k}, (0 \leq r \leq a) \tag{2.16}$$

for the core, and

$$\frac{1}{r}\frac{\partial}{\partial r}\left(r\frac{\partial T_{clad}(r)}{\partial r}\right) = 0, (a \leq r \leq b) \tag{2.17}$$

for the cladding, where k is the thermal conductivity (W/mK) and Q_0 the heat density (W/m^3). The temperature distribution can be derived from these equations by satisfying the boundary conditions: the temperature and their derivatives must be continuous across the boundaries. In addition to that, considering Newton's law of cooling, $T(r = b)$ must satisfy

$$\frac{dT_{clad}(r = b)}{dr} = \frac{h}{k}\left(T_c - T(r = b)\right), \tag{2.18}$$

where h is the convective coefficient that defines the efficiency of the cooling at the fiber surface in contact with the air, and T_c is the coolant tem-

perature. The equation describing the core and cladding radial temperature distribution are then [24]:

$$T_{core}(r) = T_c + \frac{Q_0 a^2}{4k}\left[2\ln\left(\frac{b}{a}\right) + \frac{2k}{bh}\right] + \frac{Q_0 a^2}{4k}\left(1 - \left(\frac{r}{a}\right)^2\right), (0 \leq r \leq a) \tag{2.19}$$

$$T_{clad}(r) = T_c + \frac{Q_0 a^2}{2bh} - \frac{Q_0 a^2}{2k}\ln\left(\frac{r}{b}\right).(a \leq r \leq b) \tag{2.20}$$

These equations are plotted in Fig. 2.6(b) for a fiber that is cladding pumped with 150 W of power at 915 nm and using a convective heat transfer coefficient h of 1.35·10^{-2} W/cm^{2}K, which is typical for fibers passively cooled in air. The thermal conductivity k is taken to be 1.38·10^{-2} W/cmK and the ambient temperature T_c is set to 303 K. The fiber has a core diameter of about 20 μm and a cladding diameter of approximately 125 μm. Moreover, the heat generation is assumed to be caused only by the quantum defect (0.12) given a heat load of Q_0=1.7 W/m^3.

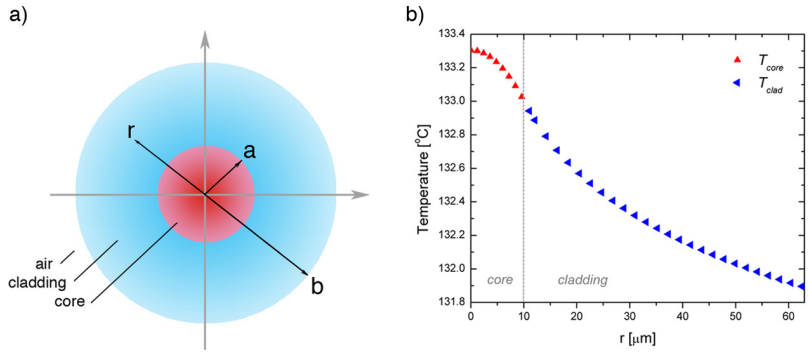

Figure 2.6: (a) Geometry of the modeled fiber. (b) Radial temperature distribution in the core and cladding region for a fiber with a heat load of Q_0=1.7 W/m^3 air cooled by natural convection.

The maximum temperature is reached at the center of the core, and from this point, it moderately decays with a rate proportional to r^2 in the core and logarithmically in the cladding. The results shows that the temperature at the outer edge of the cladding $T_{clad}(b)$ is only ~1.5 °C lower than at the center of the core. This means that at these temperature levels, $T_{clad}(b)$ can represent well the fiber core temperature when the fiber is held in air, and it can be calculated with the expression of [24]

$$T_{clad}(b) = T_c + \frac{Q_0 a^2}{2bh}. \tag{2.21}$$

In publication III, the fiber temperature is measured at the outer surface of the cladding by a thermal camera. In light of the result presented in

Fig. 2.6, and under the same cooling conditions, the fiber core temperature is approximated well by the temperature at the outer surface.

2.5.2 Large mode area fibers

Engineering techniques to avoid the onset of nonlinear and thermal effects, which sets a limit on power scaling of high power fiber lasers, have been extensively researched over the last years. An effective method to raise the threshold of nonlinearities consists of using innovative fiber designs with higher effective mode area, while maintaining single-mode operation. Initially, this was accomplished by increasing the core diameter while reducing the NA in order to maintain single-mode operation, according to V < 2.405 [52]. The counterparts of this approach are weak guidance and high bend loss. In fact, the minimum NA that can be used in practice is about 0.05, resulting in a core diameter of $\sim$15 μm for a wavelength of 1 μm. It should also be noted that very low values of the NA would require high accuracy in controlling of the refractive index profile, which complicates the fiber fabrication. Moreover, in double cladding fibers, increasing the fiber core diameter (for a fixed inner-cladding diameter) also results in an improved pump absorption.

Surpassing the single-mode restriction permits power scaling by working with step-index fibers with V > 2.405. However, the use of techniques that ensure a single-mode operation become necessary. For example, the application of bending losses can be used [53, 54], which takes advantage of the fact that the fundamental mode is the least sensitive to bend loss attenuation. Therefore, propagation of higher-order modes can be suppressed by a correct selection of the fiber coiling diameter [55]. Another approach to ensure the single-mode operation is a proper design of the rare-earth dopant distribution, thus obtaining preferential gain to the fundamental mode [56–59]. Single-mode operation can also be favored by selective excitation of the fundamental mode [60]. This can be accomplished by, e.g., under filling the optical fiber's acceptance cone or by inserting sections of a tapered fiber inside the laser cavity [61]. By the implementation of the aforementioned methods, the effective mode area in fiber laser systems with single-mode operation has increased from below 100 μm^2 (for a standard SMF) to values of hundreds or thousands of μm^2, with core diameters of at least 40 μm [19, 62, 63].

Besides the techniques mentioned above, more sophisticated fiber designs such as photonic crystal fibers (PCFs), chirally coupled core (CCC)

fibers, and leakage channel fibers (LCFs) [64] have been developed to go beyond the typical core diameters of LMA fibers. A PCF, drawn typically from a stack of capillaries, can reach a core diameter of up to 100 μm and still behave as a SMF, due to a better control of the refractive index [65–67]. However, the practicality of these fibers is compromised beyond core diameters of 40 μm, because they need to be kept straight due to bend losses. Moreover, CCC fibers, which have a straight central core for signal propagation and another helical satellite core around, are designed to resonantly couple the higher order modes to the satellite core. This leaves the fundamental mode unaffected [68].

2.5.3 Optimization of the core material

Increasing the core material absorption by means of enhancing the RE-dopant concentration N (in ions/m^3) leads to a linear reduction of the required fiber length. Hence, higher levels of dopant concentration are beneficial for power scaling due to further decrease of nonlinear effects. However, heavy RE-doping also suffers from some downside effects. RE-ions are incorporated in silica glass by adding network modifiers such as Al_2O_3 and P_2O_5 that improve the RE solubility [69, 70]. Unfortunately, the extra refractive index inhomogeneities introduced by the RE-dopants and co-dopants increase Rayleigh scattering loss. In addition to that, the corresponding increase in NA needs to be compensated by the use of index decreasing co-dopants (such as boron and fluorine).

High doping concentration may also lead to the formation of clusters of RE-ions, resulting in quenching processes that can reduce the gain and power efficiency of the material [71]. This effect takes place, for example, in Er-doped fibers, where different well described processes involving energy transfer between Er-ions (such as energy-transfer upconversion) result in decreased efficiency [1]. On the other hand, the Yb-ion in principle does not suffer from ion-to-ion energy transfer and upconversion processes due to the simple energy level structure. However, the gain efficiency of Yb-doped fibers is strongly degraded in fibers highly doped with Yb [72]. This troublesome effect was attributed to quenching processes induced by the formation of clusters.

Another process based on interaction of Yb-ions is known as a cooperative luminescence [73]. Two closely located Yb^{3+} ions relax simultaneously to their ground state resulting in the emission of a photon with a combined energy in the visible wavelength region ($\sim$500 nm). This effect

is relatively weak, and it is not considered as a threat to the efficiency of Yb-doped fibers [41]. However, since the cooperative luminescence depends on the degree of clusterization, it has been proposed as a method for characterizing clustering and other related effects, such as photodarkening [74–76].

3. Fabrication of rare-earth doped fibers

The methods used to fabricate rare-earth doped (RE-doped) fibers are, in general, variations of the manufacturing techniques used to produce conventional low-loss silica (SiO_2) based telecommunication fibers [1]. The first step of the manufacturing process is related to the fabrication of the core soot. The second step entails the fabrication of the so called preform, a macroscopic scale glass rod that defines the final refractive index profile and core/cladding ratio of the fiber. Preforms can vary in size over a wide range, from few centimeters (specialty fibers) up to tens of centimeters in diameter [77], with lengths from tens of centimeters to meters. In the final step this preform is drawn to a fiber.

The core soot is typically fabricated by vapor deposition methods that satisfy the requirements of high purity and precise control of the process. Depending on the chemical reaction used to produce the submicron silica particles the process is differentiated between hydrolysis and oxidation:

$$SiCl_4 + 2\,H_2O \rightarrow SiO_2 + 4\,HCl \qquad \text{(Hydrolisis)}$$

$$SiCl_4 + O_2 \rightarrow SiO_2 + 2\,Cl_2 \qquad \text{(Oxidation)}$$

In a process based on hydrolysis, $SiCl_4$ vapor is directed into an oxygen-hydrogen flame to induce a reaction with water molecules, which results in the formation of submicron particles of SiO_2 that are collected in a rotating target. The soot is then pre-treated at a high temperature to reduce the content of OH. The main fabrication processes based on hydrolysis are the outside vapor deposition (OVD), the vapor axial deposition (VAD), and the direct nanoparticle deposition (DND). In the OVD process the silica particles are deposited on a rotating target rod, with the burner traversing back and forth [78]. After the deposition, the target rod is removed and the soot-preform is then consolidated into a solid glass preform in a

high temperature furnace. VAD is similar to OVD, but the deposition occurs at the end of a rotating rod that slowly recedes from the burner with an advantage that very long preforms can be made [79]. DND is also a type of an outside soot deposition, but in this case the doping materials are fed in liquid and vapor phase directly to the oxygen-hydrogen flame [80, 81].

In a process based on oxidation, $SiCl_4$ reacts with oxygen to produce silica particles that are deposited inside a rotating substrate tube. The substrate is typically heated by an oxygen-hydrogen burner from the outside, with the burner traversing slowly along the rotating substrate. The fabrication process based on oxidation that has received the most attention is the modified chemical vapor deposition (MCVD) method [82].

In addition to the deposition of SiO_2 particles by hydrolysis or oxidation reactions, it is necessary to add co-dopants to modify the refractive index profile of the core and in some cases the cladding. Examples of index increasing co-dopants are germanium, phosphorus, and aluminum, and examples of index decreasing co-dopants are boron and fluorine [1]. These co-dopants can be incorporated in the soot by using highly volatile halides (e.g. $GeCl_4$) as precursors that can react during the deposition by hydrolysis or oxidation, similarly as $SiCl_4$.

Fabrication of RE-doped fibers requires the incorporation of RE-ions into the core material during the silica deposition or in a separate phase of the fabrication process, prior to sintering and consolidation of the silica soot. Direct doping of RE-ions during the soot deposition (by hydrolysis or oxidation) is less straightforward compared to the incorporation of the index modifiers (e.g. GeO_2) due to the low volatility of the halide compounds of RE-ions, such as $ErCl_3$ or $NdCl_3$ [82]. Different methods, suitable for both hydrolysis and oxidation processes, have been implemented in order to circumvent this problem. For example, placing the low vapor pressure source close to the reaction zone or utilizing alternative vapor sources such as aerosols or high vapor pressure organic compounds have been demonstrated [1, 82]. An interesting example is the use of RE-chelates as highly volatile RE precursors (e.g. based on a beta-diketonate ligand) in combination with a modified MCVD system. The dopant precursor can be delivered to the MCVD system by a tube heated to about 200 °C. Fibers with a high doping level in excess of 10 wt% of Yb_2O_3 and low background losses could be prepared by this method [83].

As an alternative to the vapor phase doping methods, incorporation of

RE-ions by liquid-phase techniques is widely used [82]. Among those techniques, the most important method is the well-established solution doping technique typically used in combination with the MCVD system.

The three state-of-the-art techniques used in the fabrication of RE-doped fibers are: i) the MCVD technique with doping by RE-chelates, ii) the MCVD technique with solution doping and iii) the DND process. The latter two manufacturing processes are described below in more detail.

Following the fabrication and doping of the core soot preform, the porous soot is sintered at a high temperature to form a transparent glass before collapsing it into a solid rod. The core/cladding ratio of the resultant fiber is defined by the preform. Therefore, in order to achieve the designed core/cladding ratio it is common to modify the cladding thickness by sleeving the rod in a glass tube. In double clad fibers, the cladding is typically machined to a desired shape.

The last step of the manufacturing process is the fiber drawing. The preform is loaded vertically at the top of a fiber drawing tower. The tip of the preform is heated by a furnace at a temperature between 1950-2200 °C. When this temperature is reached, the glass melts and a tip is formed that starts elongating due to gravity. The fiber is pulled down by a series of rollers called capstans and the outer diameter of the fiber is controlled by precisely adjusting the preform feed rate, the furnace temperature and the fiber draw rate. Finally, once the fiber cools down, it passes through one or multiple cups with coating polymers and through UV-curing furnaces in the case of UV-curable polymers before being spooled.

3.1 MCVD with solution doping method

As mentioned above, the process begins with the deposition of SiO_2 particles inside a silica tube by the MCVD process. The deposition is carried out at relatively moderate temperatures, so that the silica particles form an unsintered porous soot layer. The substrate tube is then removed from the lathe and soaked in an aqueous solution containing a RE-salt, which is allowed to impregnate the porous layer for nearly an hour before draining the solution [15]. Index-increasing dopants can also be added to the aqueous solution. After that, the tube is transferred back to the MCVD system and it is carefully dried at a high temperature ($\sim$600-1000 °C) in the presence of a flow of chlorine and oxygen mixture [1]. Following drying, the soot is sintered and collapsed in the usual manner.

The fabrication of LMA fibers with low NA and core diameters of typically more than 20 μm requires the deposition of thick core soot layers and an accurate control of the refractive index profile of the doped core. This is achieved by repeating several times the process cycle consisting of soot deposition, doping, drying and sintering of the soot. After several cycles, large doped cores with multiple layers are obtained [1, 84]. MCVD with solution doping method has been shown to be suitable for producing highly doped Yb fibers with large cores. In [19] a fiber fabricated with this method with a core diameter of 40 μm and an NA below 0.05 was successfully used to build a fiber laser generating 1.36 kW of continuous-wave output power at 1.1 μm with a slope efficiency of 83% and near diffraction-limited beam quality.

3.2 Direct nanoparticle deposition (DND)

DND is a well-proven fabrication method developed at nLIGHT Oy (Finland), which has been positioned as an alternative to the MCVD method in manufacturing commercial laser fibers. DND differentiates from other OVD processes in that a broad variety of raw materials can be fed directly to the oxygen-hydrogen flame, providing higher flexibility and allowing the incorporation of materials with very different vapor pressures. The glass is doped in-situ while the silica particles are formed and deposited to a target mandrel, thus clustering tendency is low [80, 85]. The size of the doped silica particles can be adjusted between 10 and 100 nm providing a high flexibility in the glass composition with hundreds of layers. The large number of layers allows good control of the refractive index profile, and RE and index-increasing dopant profiles in the fiber core. After the deposition phase, the soot is inserted into a furnace for drying. Following this, the soot is ready for sintering and collapsing to a preform. Fibers with excellent mode behavior have been fabricated with this process [86]. Furthermore, this method has been shown to be highly suitable for producing laser fibers with non-step-index profiles or partially doped cores (e.g. confined-doped Yb LMA fibers), which is of great importance in fiber laser engineering [59, 81].

3.3 Current limitations

MCVD in combination with the solution doping method is the most common technique in the fabrication of laser fibers. Despite the progress made with this fabrication technique [19], it is not exempt from some drawbacks. To achieve complex core structures, several core layer depositions are required. This implies that the soot preform has to be removed from and reassembled to the lathe multiple times. As a result of that, the usable length of the preform is reduced and, on the whole, the fabrication process becomes rather time consuming and expensive. As a consequence, the number of core layers observed in commercial fibers is typically relatively low, limited to about 10 [80, 81, 84]. The low number of core layers affects the production of active fibers by decreasing the degree of accuracy and flexibility of the dopant profiles, and consequently, the refractive index profile.

Recently, various alternatives to the solution doping compatible with the MCVD process have been proposed [84, 87–89]. These techniques differentiate from the previous, already available gas-phase techniques, in that the incorporation of the RE-doping is improved for allowing higher concentrations with increased uniformity and reduced clustering. Additionally, these methods eliminate repeating the quartz tube removal from and the reassembly in the lathe. Boyland et al. developed a system based on the high volatility of lanthanide chelate complexes at moderately low temperatures that allows high RE-doping when the chelates are heated in a crucible directly within the MCVD preform [87, 88]. Since the incorporation of RE-ions and co-dopants occurs simultaneously with the silica deposition, a further advantage is the possibility of reduced RE-ion clustering compared to the standard solution doping technique. Sekiya et al. reported on the use of low vapor pressure organic compounds (e.g. $Yb(DPM)_3$) in an improved gas-phase delivery system [89]. By means of this technique large core area Yb- and Al-doped silica preforms were produced with more than 40 deposited layers and a rather uniform dopant concentration profile. An alternative to these gas-phase doping techniques consists of an in situ soaking of the porous soot with a thin layer of dopant solvent with the substrate in the lathe, and drying the solution by vaporization [84]. This technique permits the deposition of multiple layers in a reasonable time making this method, compared to the normal solution doping, more appropriate for fabrication of large-area

core fibers.

Despite the advantages mentioned above, it has not been reported that any of these recently proposed techniques have been widely implemented. In this dissertation, a new fabrication method of producing Yb-doped fibers is presented. It combines the well-established MCVD process with the ability of atomic layer deposition (ALD) of depositing uniform thin films of RE oxides. This method is described in detail in Publication VI and in Chapter 7.

4. Photodarkening in Yb-doped fibers

The term photodarkening refers to the increase of transmission loss in a gain medium caused by irradiation of light at a certain wavelengths. In Yb-doped fibers photodarkening is manifested as a spectrally broad transmission loss centered at the visible wavelengths and extending up to the pump and signal wavelength region [90–92]. It is believed that the formation of photodarkening is related to the creation of color centers. In glass, color centers are created when electrons and holes generated through excitation are trapped in a defect of the glass matrix, causing an additional absorption to the transmitted light [93]. In a fiber laser or amplifier application photodarkening is mainly driven by the energy of pump and signal photons in interaction with the Yb-doped core of the fiber [91]. However, the same damage can be induced also by UV light [92, 94] and 488 nm irradiation [95].

The shape of the photodarkening loss spectrum was observed to be constant with progressing photodarkening [91]. Koponen et al. determined that the induced loss at 633 nm was 71 times higher than at the signal wavelengths 1040-1070 nm, and it was corroborated for 22 different fibers with similar composition. However, the photodarkening signature is dependent on several material parameters such as the composition and processing of the glass [96].

Photodarkening has also been observed in silica fibers doped with other RE-ions such as Tm^{3+}, Ce^{3+}, Pr^{3+}, Eu^{3+} and Tb^{3+} [97–101]. In these cases, photodarkening has typically been attributed to the formation of color centers and photoionization induced by UV photons, which could be emitted by a RE-ion previously excited to a high energy state through a multiphoton absorption process. Owing to the simple energy level diagram of Yb^{3+}, the mechanism driving photodarkening in Yb-doped fibers may follow a different path. Initially, it was hypothesized that a UV pho-

ton could be emitted via multi-excitation of Yb clusters [91, 92]. Despite the models presented to explain the photodarkening process up to these days, the mechanisms responsible of the formation of color centers in Yb-doped fibers are still not fully understood.

4.1 Inversion dependence

The dependence of the photodarkening on the population inversion level was first observed in Yb-doped fibers by Koponen et al. [27]. In this study, the progress of photodarkening was measured with time at different inversion levels by pumping short fiber samples, and the rate of change was observed to increase with enhanced inversion. The relation of the rate of change with other parameters like e.g. the pump power was neglected based on the observation that by fully inverting the fiber sample, the photodarkening decay curve was no longer dependent on the pump power. This dependence of the photodarkening on the inversion was also observed by Kitabayashi et al. by irradiating a 43 cm long sample using two pump diodes with different wavelengths (i.e. 940 and 976 nm) [102]. The excess loss measured after 100 min of pumping was shown to vary only with the population inversion regardless of the pump wavelength used, and the rate of change followed a second-power dependence with the inversion.

A more accurate and flexible measurement method for determining the temporal characteristics of photodarkening as a function of the inversion was presented in [91]. A key feature of this measurement method is the use of cladding pumping instead of core pumping, which is capable of inducing a radially and transversally homogeneous inversion in fiber samples with a large range of core diameters [44, 45]. The temporal characteristic curve of photodarkening could not be described by a single exponential function. Instead, the data results were fitted well by a stretched exponential function. From this expression any physical interpretation is very difficult, but it associates the photodarkening decay curve, measured under time-invariant pump power, to a time constant. The inverse of the time constant ($1/\tau$) was observed to be proportional to a power law of the population inversion [91],

$$\frac{1}{\tau} \propto (N_2)^n. \tag{4.1}$$

The exponent factor n, also named the ion dependence factor, has been

studied by several groups and it has been reported to have a value between 3 and 7 [45,91,103,104],[Publication IV]. This discrepancy between the different studies is analyzed in detail in section 5.6. In an application using an Yb-doped fiber, e.g. a fiber laser or an amplifier, the implications of the photodarkening effect in the device performance are closely related to the induced inversion, which varies depending on the application. Therefore, in applications using lower inversion, such as a cladding pumped CW laser ($\sim$5-10% inversion), the device can run for a long period of time before severe performance degradation due to photodarkening. An opposite case applies to applications that exhibit typically a high inversion such as an amplifier setup [44].

4.2 Bleaching

Thermal bleaching of photodarkening was for the first time reported by Jasapara et al. [105]. A fiber sample pre-photodarkened by pump irradiation at 976 nm was thermally treated with a complete recovery occurring at 500 °C. By using a similar approach, another group showed full bleaching at lower temperatures (400 °C). In Publication II, a method to determine the activation energy associated with the thermal recovery of the photodarkening losses was presented (see section 4.4). This method can be implemented to calculate the combination of values of temperature and exposure time that are necessary to achieve a partial or a complete loss recovery.

Light-induced bleaching (or the photobleaching), was also reported to reverse the photodarkening effect in Yb-doped fibers. Manek-Hönninger et al. used UV light at 355 nm with a pulse energy of 90 μJ to successfully recover the absorption spectrum to nearly its pristine state. Furthermore, a comparison of the lasing properties between the photo-bleached and the pristine sample showed very similar slope efficiency, even after several cycles of photodarkening and photo-bleaching [106]. Guzman Chávez et al. also detected partial bleaching under 1 mW of 543 nm irradiation of a pre-photodarkened sample. They hypothesized that photodarkening and photobleaching can be explained in terms of light-induced $Yb^{3+} \leftrightarrow Yb^{2+}$ conversion processes [107]. Evidence of equilibrium photodarkening states dependent on the pump power was presented by Jetschke et al. [104]. Interestingly, for a given fiber sample photodarkened up to the equilibrium level, extra pumping at lower pump power resulted in a partial bleach-

ing of the induced losses, with the loss level progressing towards a new equilibrium state. This reduction of the loss was attributed to the pump power itself, i.e. photobleaching by 915 nm irradiation. It was concluded that the equilibrium loss level depends on the fraction of excited Yb-ions. In a more recent study, partial photobleaching of pump-induced photodarkened samples was also observed with 633 nm irradiation [108]. By this approach, only roughly 80% of the total losses could be bleached suggesting that a fraction of the color centers may require higher activation energies. The percentage of bleached photodarkening was observed to be lower for samples pre-photodarkened at a level close to saturation, and it was identified that the defects created during the last period of the photodarkening process require higher energy to be bleached.

4.3 Combined photodarkening and thermal bleaching measurement

The applied measurement approach used in this thesis for characterization of photodarkening and thermal bleaching is presented schematically in Fig. 4.1. In a photodarkening measurement, the core absorption coefficient change $\Delta\alpha$ in dB/m, normalized to the pristine fiber absorption, is monitored by a probe during cladding pumping at a wavelength of 915 nm. The probe generated by a halogen lamp is launched to the core of a single cladding multi-mode fiber (MMF), after being filtered (typically at 600 nm) and modulated by a chopper for lock-in detection. An MMF coupler is used to extract a small portion of the light as a reference to minimize measurement errors due to power fluctuations of the halogen lamp, enabling very long measurement durations. The pump laser pigtail is spliced to the setup and the pump light is coupled to the cladding of the sample through a pump combiner, so that the pump light and the probe propagate in opposite directions. The non-absorbed cladding pump light is removed by a mode stripper and a single-cladding passive fiber ($\sim$2 m in length). This prevents damaging of sensitive components by the strong pump and avoids saturation of the detectors. In addition, the mode stripper and the single cladding fiber also remove the cladding modes of the probe light that have low overlap with the core and could underestimate the loss measurement. More details of the setup were presented in Publication IV and in a previous conference paper [109].

A typical combined photodarkening and thermal bleaching measure-

ment consists of a photodarkening rate measurement and a subsequent thermal treatment that recovers the sample to its pre-photodarkening state. For thermal bleaching measurements, the pump power is turned off and a miniature furnace (MHI Inc. model FIBHEAT) is moved over the sample fiber and is aligned so that the fiber is positioned inside the furnace hot zone. The fiber temperature is monitored by using a K-type thermocouple that is placed next to the fiber inside the furnace. To avoid fast temperature changes in the fiber, which could damage the glass structure, the fiber is placed inside the furnace during the ramp up/down (20 to 30 °C/min.) of temperature.

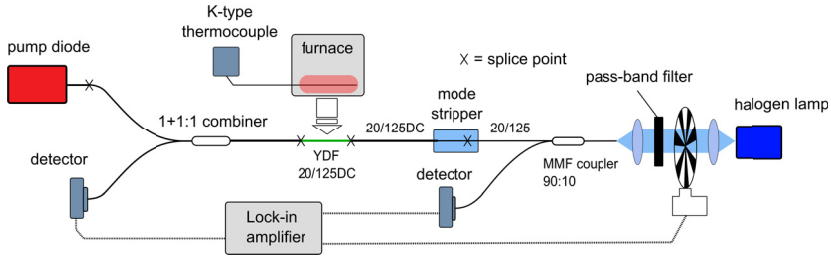

Figure 4.1: Experimental setup for photodarkening and thermal bleaching measurements. YDF: Yb-doped fiber. DC: double cladding fiber. MMF: multi-mode fiber. (Publication IV)

Figure 4.2 presents a combined photodarkening and thermal bleaching measurement monitored at 600 nm. For the fiber used, the total recovery of the induced losses ($\geq$ 99.99%) was achieved by heating the fiber sample up to 630 °C for 5 min. The necessary applied temperature and exposure duration, i.e., the energy, to fully recover a fiber can be calculated using the analysis presented in Publication II (see section 4.4). To show that the recovery after the thermal bleaching occurs not only at 600 nm, but in a broader spectral range, the transmission spectrum was measured before and after the thermal exposure. Inset graph in Fig. 4.2 shows the derived $\Delta\alpha$ (in dB/m) as a function of the wavelength, showing that the sample was completely recovered in that range.

The developed approach enables carrying out multiple measurements over the same sample, eliminating uncertainties related to a change in the sample, e.g. no inaccuracy of the fiber length, no longitudinal variations in doping homogeneity, and no geometrical variations. In Publication IV, results that validate our approach were presented. A sequence of photodarkening and thermal bleaching measurements were repeated five times under the same conditions of pump power (10.5 W), air cooling, and mea-

surement duration (20 h). The photodarkening decay curves were fitted by a stretched exponential function [110],

$$-\Delta\alpha(t) = \Delta\alpha_{sat} \cdot \left(1 - \exp\left(-(t/\tau)^{\beta}\right)\right), \tag{4.2}$$

where the $\Delta\alpha(t)$ is the absorption coefficient change in units of dB/m, the constant $\Delta\alpha_{sat}$ is the saturation parameter, τ is the time constant, and β is a parameter that ranges between 0 and 1 and is referred to as the stretching parameter. The derived statistics of the fitting parameters showed very small differences without any recognizable trend of drift. The observed differences were attributed to variations in the ambient temperature during the experiments and they do not indicate any compositional or structural changes of the glass. Figure 4.3 shows that the photodarkening decay curves overlap well and an inset table presents the statistics of the fitting parameters.

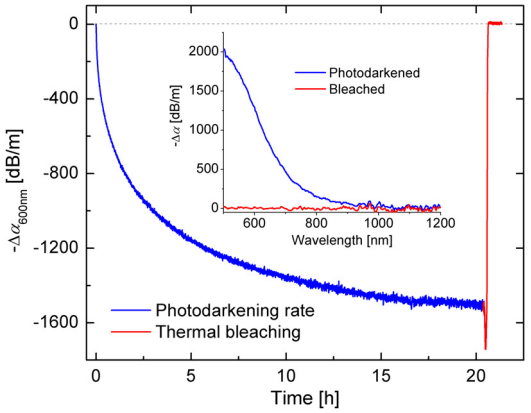

Figure 4.2: Photodarkening measured under the conditions of 10.5 W of pump power and air cooling, and a subsequently in-situ thermal bleaching measurement, i.e. the fiber is heated up to 630 °C and maintained for 5 min with slow ramp up/down (20 to 30 °C/min). Inset: Excess loss spectrum ranging from visible to IR measured before and after the thermal bleaching measurement.

In a preceding conference publication, in a similar sequence of photodarkening and thermal bleaching measurements, the fiber temperature was applied as a step function, i.e. the furnace was pre-heated to roughly 600 °C prior to the exposure of the fiber, and it was removed after the fiber recovered, letting the fiber to cool down abruptly by air cooling by natural convection [109]. The time constant of the photodarkening measurement derived from the fitting was observed to gradually increase in the subsequent two measurements, revealing a change in the glass structure due

to the fast temperature changes to which the fiber was exposed, although the fiber temperature was far from the melting temperature of glass (e.g. 1600 °C). A spectroscopy study of the fiber absorption revealed a decrease in the Yb-absorption accompanied by a loss increase at the UV region. In [111] a post-annealing of an Yb-doped fiber sample in reduced oxygen atmosphere at 900 °C for 5 hours showed similar results attributed to a conversion from Yb^{3+} to Yb^{2+}, which is in a good agreement with the aforementioned observations. These results highlight the importance of avoiding a rapid temperature change during the thermal bleaching experiments.

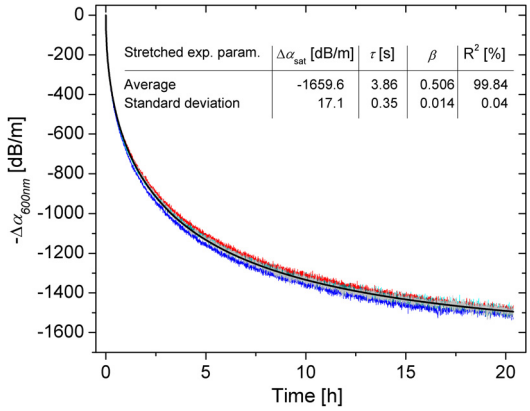

Figure 4.3: Photodarkening-induced absorption coefficient change $\Delta\alpha$ at 600 nm as a function of time for 5 subsequent experiments at 10.5 W. Inset table shows the average and standard deviation of the calculated stretched exponential parameters. (Publication IV)

4.4 Thermal activation energy

In Publication II and in a preceding conference paper [112], the activation energy associated with the thermal recovery of photodarkening-induced losses was measured using an isothermal measurement method. This method was introduced by Erdogan et al. on predicting the thermal decay of ultraviolet-induced fiber Bragg gratings (FBGs) [113]. The theoretical model was based on the assumption that carriers (i.e. an electron or a hole) excited during the UV-irradiation are trapped in a continuous distribution of energy states. The trapped charges can be freed or detrapped via thermal excitation returning the charge to the initial non-absorbing state with the rate of recovery being a function of the trap depth. This

so-called master/demarcation energy curve approach has also been applied to analyze the recovery of gamma radiation-induced loss in Yb-Er doped silica fibers [114]. Although the formation mechanism of photodarkening is very different from that used in writing FBGs, the host glass used is similar, and therefore the freed charges are hypothesized to occupy similarly a distribution of trap sites of different energy-well depths. The existence of a distribution of traps, rather than a single trap level is suggested by the broad absorption spectrum of photodarkening. Thus, the theoretical picture proposed by Erdogan et al. is expected to describe well also the mechanism driving the thermal bleaching of photodarkening. Figure 4.4 plots three isothermal thermal bleaching measurements, with the $\Delta\alpha$ normalized with α_{max}, carried out over the same undisturbed sample. The method used is the same as the one presented before, but in this case the furnace is pre-heated and stabilized at a given temperature before the fiber sample is introduced in the heat-zone, and at the end of the measurement the fiber temperature is further increased to recover the sample completely.

Central to the theoretical picture is the assumption that the (post-irradiation) population of the trap sites as a function of temperature and time is uniquely determined by a "demarcation energy" (E_d), given by

$$E_d = k_B T \ln(\nu_0 t), \tag{4.3}$$

where k_B=$8.617 \cdot 10^{-5}$ eV/K is the Boltzmann constant, and the parameter ν_0 represents the characteristic vibrational frequency at which a defect "attempts" to escape from the trap state [113]. It is convenient then to reinterpret the data from Fig. 4.4(a) in terms of the E_d, as it is shown in (b). By varying ν_0 it is possible to fit well the measured $\Delta\alpha$ on the same curve, which validates the theoretical assumption. The best fit is achieved for ν_0=2.0 GHz. The dashed line represents a simple analytical form for the dependence of the $\Delta\alpha$ on E_d, called the "demarcation energy curve". The fit parameters indicate the peak of the energy distribution, e.g. ΔE=1.32 eV for the fiber in use. The inset graph shows the initial defect energy distribution with a full width at half maximum (FWHM) of 0.31 eV. Another commercial large mode area (LMA) fiber was analyzed for comparison, resulting in ν_0=2.0 GHz, ΔE=1.50 eV and FWHM=0.34 eV. The differences in the defect energy distribution between these two fibers are not well understood, but they are likely to be related

to compositional differences or differences in the fabrication process.

There is a unique demarcation energy E_d associated with each value of $\Delta\alpha_n$, with the trap states with an energy-well below E_d being bleach, and the trap states with an energy-well with higher depth remaining unchanged. E_d is determined by a combination of time and temperature. Thus, a complete recovery of the photodarkening losses (i.e. $\Delta\alpha \leq 0.01$) occurs at energies $\geq$1.9 eV, which can be achieved with e.g. a fiber temperature of 600 °C for 47 s. It should be noted also that this result does not necessarily predict a light absorption peak at 1.32 eV, since the experiments only predict the thermal activation of trapped charges.

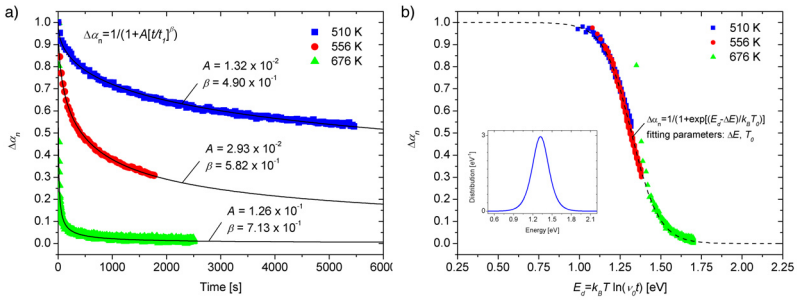

Figure 4.4: (a) Normalized absorption coefficient change $\Delta\alpha$ as a function of time for thermal bleaching measurements at three different temperatures. (b) Normalized $\Delta\alpha$ plotted as a function of the demarcation energy E_d. The attempt frequency ν_0 is set to 2 GHz. Inset graph shows the initial defect energy distribution. (Publication II)

4.5 Color center formation

Since the first reported experimental evidences of photodarkening [27], several theories have been suggested to explain the photodarkening related color center formation. Jasapara et al. suggested that the photodarkening loss is caused due to the reduction of Yb^{3+} to Yb^{2+} through a capture of excited electrons by Yb^{3+} pairs [105]. This was hypothesized after observing that a loss spectrum similar to photodarkening could be induced by exposing the Yb-doped fiber sample to a mixture of H_2 and N_2 at elevated temperatures. Guzman Chávez et al. observed a temporal decrease of the Yb^{3+} absorption peak at 977 nm with progressing photodarkening. This change in the Yb absorption was attributed also to conversion from Yb^{3+} to Yb^{2+}, implying the capture of an electron from a nearby ligand and the creation of a hole center responsible for the spectral

loss at the visible wavelengths [107]. Moreover, Koponen et al. observed a seventh order dependence of the photodarkening rate on the inversion and suggested that Yb clusters with up to seven ions can emit a single photon with combined energy that would be enough to photoionize the silicate host [91].

Engholm et al. observed the existence of a strong absorption band in the UV wavelengths for Yb-doped aluminosilicate fibers, and this absorption was attributed to several overlapping charge-transfer (CT) absorption bands [94, 111]. Excitation into a CT band located near 230 nm was attributed to the temporal formation of an Yb^{2+} ion and a bound hole [111]. A stable Yb^{2+} and a free hole were hypothesized to be generated upon excitation to a CT band located near 190 nm, resulting in the formation of color centers [94]. Excitation into this higher energy CT band was found to be correlated with the photodarkening induced losses. Moreover, the Yb^{3+}-doped SiO_2–P_2O_5 fiber showed a shift to higher energy of the CT band that correlated to the lower level of photodarkening observed in phosphosilicate fibers [115]. Yoo et al. also investigated the UV absorption band in Yb-doped fiber preforms, but here, on the contrary, the 230 nm absorption band was assigned to an Yb-associated oxygen deficiency center (ODC) [95]. Photodarkening was observed under 488 nm irradiation, assuming a two-photon absorption process. Experiments on oxygen loaded fibers showed decrease of photodarkening, which supported their hypothesis. The nature of the UV absorption band is still under debate [116–121].

Arai et al. implemented a different approach for studying the origin of photodarkening through analyzing the formation of unpaired electrons by electron spin resonance (ESR) measurements [122]. Their ESR measurements indicated that both samples irradiated by 976 nm pump light and gamma-rays mainly generate Al-oxygen hole centers (Al-OHC).

More recently, Peretti et al. reported enhanced photodarkening in a Tm codoped Yb-doped fiber pump at 976 nm, and attributed photodarkening to the formation of color centers by UV emission from Tm^{3+} ions fueled from excited Yb^{3+} ions in a multistep upconversion process [123, 124]. In a similar fiber, without Tm co-doping, analysis of UV and visible emission showed that Tm^{3+} ions can exist in an ordinary Yb-doped fiber from contaminations of the ytterbium raw material, and it was concluded that even very small concentrations of Tm (below 1 mol-ppm) could cause photodarkening. Later, Jetschke et al. published a detailed investigation on

photodarkening of a series of Yb-doped fibers with varying Tm co-doping (in a wide range; more than four orders of magnitude) [125]. Their results confirmed that a Tm concentration above 10 mol-ppm in Yb-doped fibers can assist photodarkening by accelerating the process of creation of color centers through a multistep Tm excitation and the emission of UV light. However, for lower contents of Tm (below 10 mol-ppm) the photodarkening parameters were not affected, and it was thereby concluded that photodarkening is an intrinsic feature of Yb-doped aluminosilicate fibers and not driven by Tm impurities.

4.6 Mitigation

Up to now, different methods have been used to reduce the effect of photodarkening in Yb-doped laser fibers. Nevertheless, each method may suffer from some intrinsic drawbacks. A reduction of the Yb concentration was suggested to ensure long-term operation of Yb-doped laser fibers without photodarkening [126]. However, this approach contradicts with the high pump power absorption required for power scaling. Kitabayashi et al. showed remarkable reduction of photodarkening with enhanced aluminum co-doping [102]. Aluminum (Al) is the preferred choice of co-dopant in Yb-doped silicate fibers and in other RE-doped silicate fibers, owing to its excellent capability of dissolving clustering [69]. Yb/Al-doped fibers also benefit from having high absorption and emission cross sections and good thermal and mechanical properties.

Shubin et al. studied photodarkening in Yb-doped aluminosilicate and phosphosilicate fibers [103]. Yb/P-doped fibers were observed to be much more photodarkening resistant compared to the Yb/Al-doped fibers [115]. However, P co-doping has some disadvantages such as reduction of Yb absorption and emission cross sections, high core background loss, lower softening point and increased core numerical aperture [127]. Jetschke et al. investigated photodarkening and lasing efficiency of Yb-doped fibers co-doped with aluminum and phosphorous [128]. Core composition with equal concentrations of Al and P (about 4 mol% each) was found to result in much improved photodarkening resistivity, high laser efficiency and low numerical aperture. However, the Yb absorption and emission cross sections were still lower compared to the Yb/Al-doped fibers.

Finally, a strong improvement in the photodarkening resistance of Yb-doped aluminosilicate fibers and high lasing efficiency was achieved by

cerium (Ce^{3+}) co-doping [129]. The reduced photodarkening was attributed to the ability of the Ce^{3+}/Ce^{4+} in trapping both hole- and electron-related color centers. A downside with Ce co-doping is the enhanced numerical aperture caused by the refractive index contribution of Ce.

5. The role of temperature in the photodarkening-induced loss

The photochemical processes that lead to the color center formations responsible for the measured photodarkening losses are shown to be reversible when applying heat to the damaged fiber, which enables the fiber to recover to its initial pristine state. The derived activation energy associated with the thermal recovery shows that even at moderate fiber temperatures a slow recovery is expected to take place, with the rate of recovery being directly related to the fiber temperature.

Leich et al. have studied the temperature dependence of the photodarkening kinetics under conditions of constant pump power [130]. The initial increase of loss was examined by fitting a stretched exponential function to the photodarkening measurement with the derived rate parameter ($1/\tau$) and the maximum loss level being examined as a function of temperature. The results showed that the photodarkening process accelerated almost exponentially with temperature, whereas the maximum loss level was observed to decrease progressively with temperature. Yoo et al. observed a similar trend, but in this case a complete bleaching was achieved in about one hour of pumping at 573 K [131].

In these studies, however, very little attention was paid to key parameters that are relevant to the photodarkening process. First, the effect of temperature on the distribution of the defect sites (either in presence or absence of pump power) was not accounted for. Second, neither was the role of the heat load generated by the photodarkening-induced pump power absorption, which has an influence on the fiber core temperature. Third, the effect of temperature on the population inversion, which is one of the key parameters driving the photodarkening process [91, 104], was overlooked.

This chapter is a summary of the main results presented in Publications I, III, IV, in which the above mentioned parameters were studied. This re-

search was carried out using commercially available 20 μm core diameter large mode area fibers from two different manufacturers.

5.1 Post-irradiation heat-induced darkening

In Publication I, the thermal bleaching process was studied in detail by applying triangular thermal ramp up/down cycles to a photodarkened fiber sample. Two new effects were observed to take place during the thermal cycling of a photodarkened sample when keeping the fiber temperature below the level at which the recovery initiates: i) heat-induced darkening (addressed in this section) and ii) spectral loss broadening (section 5.2). A thermal bleaching cycle was applied to a fiber sample previously photodarkened up to saturation of the losses with 15 W of pump power at 915 nm for 22 hours. The absorption coefficient change $\Delta\alpha$ monitored at 600 nm showed an increase in the absolute magnitude before the thermal recovery initiated, i.e., at a temperature of 325 °C for the fiber in use. A more rigorous study of this effect is shown in Fig. 5.1, illustrating a case in which the fiber sample was photodarkened again and gently thermally cycled between room temperature (RT) and 325 °C, before the temperature was increased to 650 °C to fully recover the fiber sample.

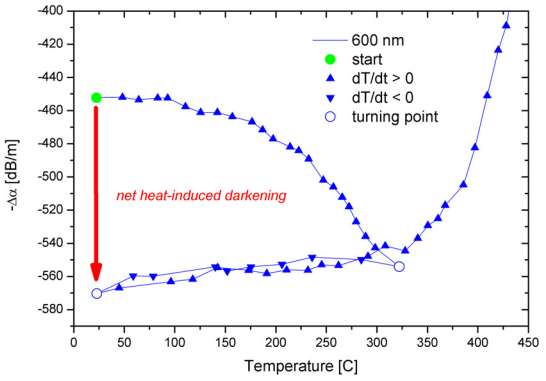

Figure 5.1: Absorption coefficient change $\Delta\alpha$ during thermal cycling between RT and 325 °C, followed by a cycle between RT and 650 °C. Heat-induced change of $\Delta\alpha$ at RT is indicated by an arrow between "start" and second "turning point". (Publication I)

The results show that starting at 100 °C the $\Delta\alpha$ increases almost exponentially until the fiber temperature reaches 325 °C. Upon cooling the fiber to RT, the $\Delta\alpha$ reaches about 570 dB/m. Thus, the post-irradiation heat-induced darkening was estimated to constitute roughly 20% of to-

tal induced losses. The same percentage change can also be derived from spectral measurements of the absorption coefficient before and after the thermal cycling between RT and 325 °C (shown in Fig. 5.2). The fiber sample can be bleached completely by a thermal cycle to ∼650 °C and back to RT. The same thermal cycle applied to a pristine sample caused no change to the $\Delta\alpha$ during the experiment, also at elevated temperatures.

Previous studies have reported a similar effect of post-irradiation increase of loss [132–134]. Sahu et al. observed a room temperature post-irradiation temporal loss growth at 1.28 μm in a 10 m Yb-doped aluminosilicate fiber sample after 488 nm irradiation [132]. In a more recent publication by the same group, this effect was again reported for a 2 m long Yb-doped aluminosilicate fiber at RT, and its temporal dynamics were seen to be enhanced by increasing the fiber temperature to 120 °C [133]. Leich et al. also observed heat-induced loss increase during non-isothermal bleaching experiments prior to the activation of thermal bleaching, which occurred at ∼230 °C. However, after reaching this temperature level, the fiber was not returned back to RT, and, therefore, the magnitude of the loss increase attributed solely to the enhancement of permanent heat-induced darkening could not be derived [134]. Furthermore, early thermal bleaching studies on photodarkening do not report any post-irradiation heat-induced darkening [103, 105]. These disagreements may be due to differences in the setup configuration or in the composition of the measured fibers.

5.2 Spectral broadening

Another thermally activated feature that affects photodarkening-induced losses found to cause non-permanent temperature dependent changes in the $\Delta\alpha$ is spectral broadening. These studies were first presented in Publication I. The magnitude of the change in the absorption coefficient was found to depend also on the wavelength used in measurements. Therefore, this effect could be more easily interpreted when the $\Delta\alpha$ was presented as a function of λ (wavelength), i.e. by performing spectral measurements. Figure 5.2 shows two spectral measurements at elevated temperatures, at 146 and 304 °C. Prior to these measurements, the fiber sample was photodarkened and thermally cycled between RT and 325 °C to generate heat-induced darkening.

The results show that at elevated temperatures the $\Delta\alpha$ spectrum is

spectrally broadened, with the wavelengths shorter than λ_0, the cross-over wavelength , exhibiting decreased losses, and the wavelengths longer than λ_0 exhibiting increased losses with increasing temperature. The magnitude of the change $d(\Delta\alpha)/dT$, in the 550-850 nm spectral range, was measured to be proportional to $\mid \lambda - \lambda_0 \mid$. For example, a change of 0.19 (dB/m)/°C at 670 nm was measured for the fiber in use. Gaussian fits to the experimental data indicate that, within the wavelength range used, the temperature dependent spectral broadening can be well described by a spectral broadening of a single absorbing species. In [134], photodarkening spectral measurements at elevated temperatures revealed a similar effect of temperature dependent spectral loss change, confirming the results presented in Fig. 5.2. However, in this study the cross-over wavelength λ_0 was observed to be at a shorter wavelength (∼550 nm), which may be explained by compositional differences between the measured fibers.

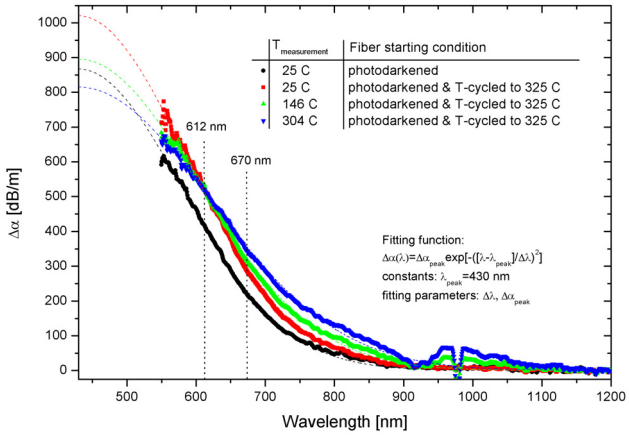

Figure 5.2: Absorption coefficient change spectra $\Delta\alpha(\lambda)$ measured after photodarkening, after thermal cycling (from RT to 325 °C and back), and at 146 °C and 304 °C (after completing the first thermal cycling sequence). Dashed lines show a Gaussian fit to the respective data sets. (Publication I)

The impact of the spectral broadening was also evaluated in the vicinity of the pump wavelength in Publication III. As seen in Fig. 5.2, the spectral measurements recorded at elevated temperatures are disturbed in the Yb-absorption region due to thermal depopulation of the ground state [135]. This effect complicates the analysis and has to be taken into account when deriving the photodarkening spectral broadening at the pump wavelength.

Accurate spectral broadening measurements at the second Yb-absorption peak, i.e. at 920 nm, were presented in Publication III. The thermal depopulation effect was extracted from the data measured prior to the onset of significant photodarkening. Figure 5.3 shows the measured Yb-absorption change due to thermal depopulation (Abs_{920nm}) and the isolated effect of the photodarkening-induced losses ($\Delta\alpha_{920nm}$) as a function of temperature. For the characterized fiber, the net increase in $\Delta\alpha_{920nm}$ versus temperature was $\sim$0.89%/°C.

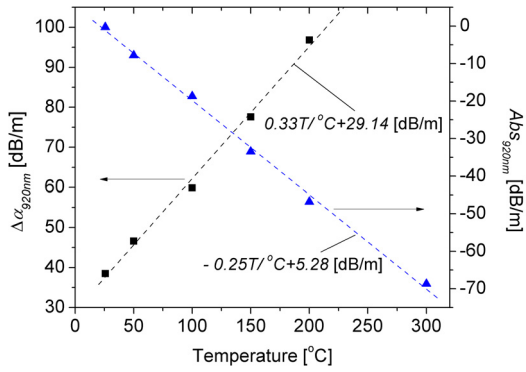

Figure 5.3: Temperature response of the absorption coefficient change at 920 nm ($\Delta\alpha_{920nm}$, primary axis) and the Yb-absorption coefficient change (Abs_{920nm}, secondary axis). Dashed lines show a linear fit to the data. (Publication III)

Despite the excellent thermal management capabilities offered by the optical fibers due to their very high surface to volume ratio, high power fiber lasers are likely to operate at a temperature substantially above the RT [136]. The results presented in Fig. 5.3 indicate that a photodarkened fiber operating at 100 °C exhibits an increase in the loss level of >50% with respect to the loss level at RT, i.e. an increase from 38.5 to 60 dB/m. Therefore, under photodarkening conditions at temperatures above RT, spectral broadening should be considered as an additional source of heat due to pump absorption. This should be taken into account when predicting the thermal load of active fibers used in high power fiber lasers.

The spectral broadening can distort photodarkening rate measurements through variations of the fiber sample temperature. To mitigate this effect, the fiber should be actively cooled. Alternatively, one could ensure that the measurement probe light is centered at a wavelength close to λ_0 (i.e. 612 nm for the fiber used in Fig. 5.2). Preferably both methods should be used to ensure accurate measurements.

5.3 Photodarkening-induced increase of fiber temperature

In Publication I, the spectral broadening was observed to take place during accelerated photodarkening rate measurements. During pump irradiation, $\Delta\alpha$ monitored at 670 nm was higher than expected from the ratio of $\Delta\alpha_{670nm}/\Delta\alpha_{600nm}$ measured from the loss spectrum at RT, and also compared to the loss level measured with the pump off. Under those circumstances, it was estimated that the fiber could reach temperatures in excess of 100 °C during the accelerated photodarkening measurements. An accurate knowledge of the fiber temperature is important to understand the photodarkening-related thermal processes that may take place during IR irradiation, namely i) the influence of the spectral broadening in the photodarkening rate measurements, ii) the activation of the heat-induced darkening, and iii) the role of the thermal bleaching throughout the photodarkening experiments.

The measurement of the fiber temperature during the recording of the photodarkening decay curves was presented in Publication III for the first time. For that, a high resolution thermal camera (FLIR A320) equipped with a microscope objective was incorporated to our experimental setup. The accuracy of the temperature measurements was estimated by a comparison of the thermal camera results to an indirect approach based on the effect of the spectral broadening of the losses that uses an external heat source. By following this approach, the accuracy of the thermal camera was estimated to be $< \pm 10$ °C for the measured temperatures.

Figure 5.4(a) presents two measurements of the absorption coefficient change $\Delta\alpha$ at 600 nm and the respective fiber temperature when using 5.7 W and 10.5 W of pump power at 915 nm. The fiber temperature was assumed to be in a steady state for each level of induced losses. This assumption was validated in a separate experiment, in which the photodarkened fiber sample reached a steady state temperature of 120 °C in a few seconds, in response to turning on a pump signal of 10.5 W. In Fig. 5.4(b) the fiber temperature increase due to photodarkening ΔT_{PD} is presented versus the product of the absorption coefficient from Fig. 5.4(a) and the pump power, $\Delta\alpha_{600nm}P_{pump}$ (dBm^{-1}W). The thermal loading associated with the quantum defect ΔT_{QD} was determined before the onset of significant photodarkening, which allowed us to isolate the effect of subsequent heating due to photodarkening effect ΔT_{PD}. Some important observations were made from Fig. 5.4. The fiber temperature recorded

shows a clear relationship between the photodarkening losses measured at 600 nm and the fiber thermal loading. Towards saturation of the losses, the fiber temperature exceeding 120 °C is measured for a pump power of 10.5 W, which possibly activates the temperature related photodarkening processes mentioned above. The relation between the ΔT_{PD} and the product of the loss level and the pump power ($\Delta\alpha_{600nm}P_{pump}$) is approximately linear.

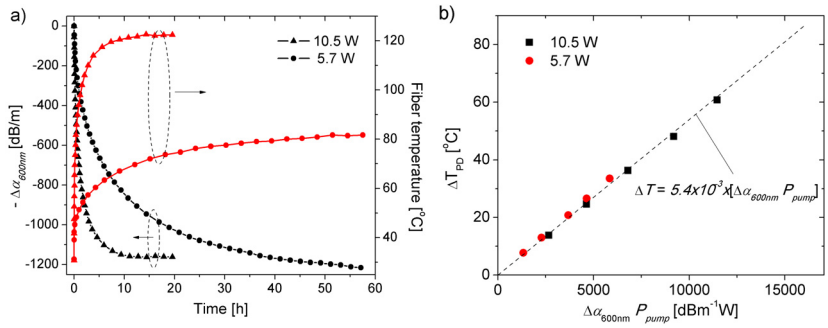

Figure 5.4: (a) Photodarkening-induced absorption coefficient change $\Delta\alpha$ at 600 nm and simultaneous increase of fiber temperature (measured by a thermal camera) (secondary y-axis) as a function of time. (b) Photodarkening induced temperature rise ΔT_{PD} versus $\Delta\alpha_{600nm}P_{pump}$. ΔT_{QD} was measured to be approximately 17 °C and 30 °C at a pump power of 5.7 and 10 W, respectively. (Publication III)

5.4 Thermal model

In publication III, a model was implemented that predicts the fiber temperature as a function of the pump power in a constant concentration of defect sites. The model is based on a previously published 2-dimensional model by D. C. Brown and H. J. Hoffman [24], which simulates the radial temperature distribution of a double cladding fiber. This model assumes that the core and the cladding region have the same thermal properties, and that the heat load is generated uniformly in the doped core of the fiber. This thermal model was presented in section 2.5.1, and it was concluded that the fiber core temperature is approximated well by the temperature at the outer surface of the cladding, for the given conditions of cooling by natural convection.

Brown and Hoffman considered only the heat generated by the quantum defect. In this study, however, two sources of heat were taken into account:

i) the absorbed pump that is dissipated as heat due to the quantum defect and ii) the fraction of the pump power absorbed by the photodarkening losses. Therefore, the heat power density Q_0 can be defined as

$$Q_0 = \frac{\eta P_{abs}(T) + P_{lost}(T)}{V_{core}}, \tag{5.1}$$

where Q_0 is in units of W/m^3, η is the fractional quantum defect, P_{abs} is the Yb-absorbed pump power, P_{lost} is the lost pump power due to photodarkening, and V_{core} is the core volume of the sample. P_{abs} and P_{lost} can be calculated using the expressions

$$P_{abs}[W] = P_{pump}(1 - 10^{-\alpha_{915nm}\Gamma L/10}), \tag{5.2}$$

$$\alpha_{915nm}[dB/m] = 4.343 N_c(N_1\sigma_a(T) - N_2\sigma_e), \text{ and} \tag{5.3}$$

$$P_{lost}[W] = P_{pump}(1 - 10^{-\Delta\alpha_{920nm}\Gamma L/10}), \tag{5.4}$$

where N_1 and N_2 are the normalized population for the ground state and the excited state, respectively; N_c is the Yb-ion concentration in units of ions/m^3; Γ is a factor that defines the overlap of the pump signal with the fiber core; L is the fiber length; and σ_a and σ_e are the absorption and emission cross sections at the pump wavelength. N_2 is also dependent on σ_a, and can be calculated using the equations presented in section 5.5. Since σ_a is linearly proportional to the Yb small-signal absorption, the temperature dependence is accounted for by using the linear fit to the Abs_{920nm} shown in Fig. 5.3, as a normalized percentage change (see section 5.2). The additional increase of loss due to the temperature dependent spectral broadening of photodarkening is accounted for by using the linear fit to the measured $\Delta\alpha_{920nm}$ in Fig. 5.3.

Note that to ensure a stable concentration of defect sites, this study was carried out with a fiber in a state of saturation of photodarkening losses ($\Delta\alpha_{600nm}$=1200 dB/m) induced by 10.5 W of pump at 915 nm. Figure 5.5 shows the simulated and measured fiber temperature at the outer surface of the cladding as a function of the pump power. The convective coefficient h is the only parameter that is adjusted to fit the simulation with the measured data, with h = 1.35·10^{-2} W/cm^{2}K giving the best fit. The simulation follows the measured data well up to 9 W of pump power. However, at higher powers the simulation shows a near exponential trend that deviates from the measurement. The reason for this discrepancy is not fully understood yet, but it might be related with the approach used

in the characterization of the spectral broadening. Prior to that characterization, the fiber temperature was thermally cycled between RT and 210 °C with the heat-induced darkening taking place. Here, the temperature increase was induced by an external heat source in absence of pump light [Publication I], [133, 134]. On the contrary, the measurement of the fiber temperatures induced by pump power cannot be carried out in presence of the heat-induced darkening. Although the heat-induced darkening represents a small fraction of the total losses, and it has been suggested that the losses are originated from the same type of defects, the existence of different absorbing species cannot be ruled out. This would imply a change in the spectral broadening that could not be characterized with the external heat source.

Two other important observations can be made from Fig. 5.5. First, the contribution of the quantum defect is relatively small compared to the heat load generated by photodarkening. Second, the model data set, in which spectral broadening is neglected, illustrates the importance of including this effect when predicting the fiber thermal load.

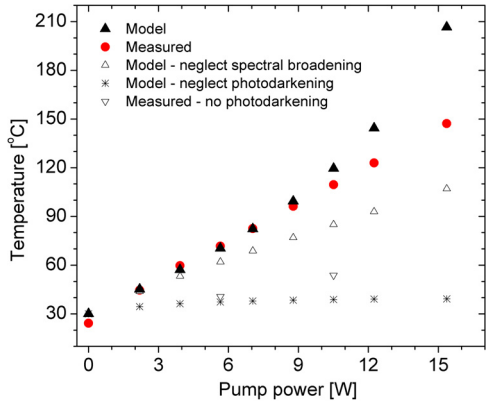

Figure 5.5: Modeled and measured fiber temperature as a function of pump power. Modeled data is fitted to the measured temperature using the convection coefficient h as the only adjustable parameter. The same value of h is used for all subsequent calculations. (Publication III)

5.5 Temperature dependence of inversion

The fiber population inversion is related to at least two parameters that are affected by the fiber temperature, namely the Yb-absorption cross section due to thermal depopulation of the ground state, and the upper state

lifetime [135, 137]. In Publication IV the influence of temperature on the population inversion is studied in a short fiber sample under cladding pumping at 915 nm. Owing to the short length of the fiber sample, the ASE can be neglected (see section 2.4) and the normalized inversion N_2 can be approximated by the expressions

$$N_2 = \frac{\sigma_a(T)}{\sigma_a(T) + \sigma_e} \frac{1}{1 + I_{sat}/I_p}, \tag{5.5}$$

$$I_{sat} = \frac{h_p v_p}{(\sigma_a(T) + \sigma_e)\,\tau_{21}(T)}, \text{ and} \tag{5.6}$$

$$\tau_{21}(T) = \tau_{21} - 0.027\Delta T/100, \tag{5.7}$$

where I_p is the pump intensity, h_p is the Plank constant, v_p is the pump frequency, and τ_{21} is the upper state lifetime [44]. The temperature dependence of τ_{21} is taken into account by a linear approximation of the results observed by Newell et al. [137]. Figure 5.6 illustrates the temperature dependence of the fiber population inversion in a range of temperatures from RT to 300 °C, at a constant pump power of 10.5 W. The plot indicates a noteworthy change in the inversion level with a drop of almost 15% when the fiber temperature is elevated up to 300 °C.

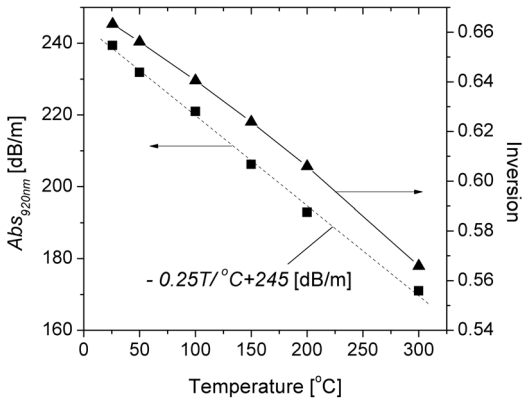

Figure 5.6: Temperature response of Yb-absorption coefficient at 920 nm (primary axis) and the derived inversion level at 10.5 W of cladding pump power (secondary axis). (Publication IV)

Previous publications on photodarkening experiments (by pump irradiation at 976 nm) at elevated temperatures assume a very small influence of the temperature to the population inversion [130, 131]. Leich et al. reported on characterization of photodarkening of Yb-doped fibers in a wide temperature range from 77 to 773 K [130]. They assume that the Yb-

inversion is maintained at a constant level of 46% for all experiments. In a similar study, Yoo et al. consider a population inversion of 47% to be constant with about 1% variation within a temperature range of 300 to 573 K [131]. However, taking into account that the thermal depopulation of the ground state affects similarly the 915 and 976 nm absorption peaks [135], the results presented in Fig. 5.6 indicate substantial variations in the inversion for the temperature range used in the results presented in [130, 131]. Therefore, the change in the inversion should be considered in the analysis of the temperature dependence of the photodarkening parameters.

5.6 Ion dependency discrepancy

The photodarkening-induced increase of the fiber temperature that occurs during the course of photodarkening measurements has been shown to affect the different photodarkening parameters (e.g. the photodarkening rate ($1/\tau$) and the saturation loss level), and also the inversion level. Thus, the photodarkening ion dependence, extracted from the relation of $1/\tau$ with the inversion, should be determined from the measurements carried out under the same isothermal conditions at temperatures below the activation of the thermal bleaching process (e.g. at RT).

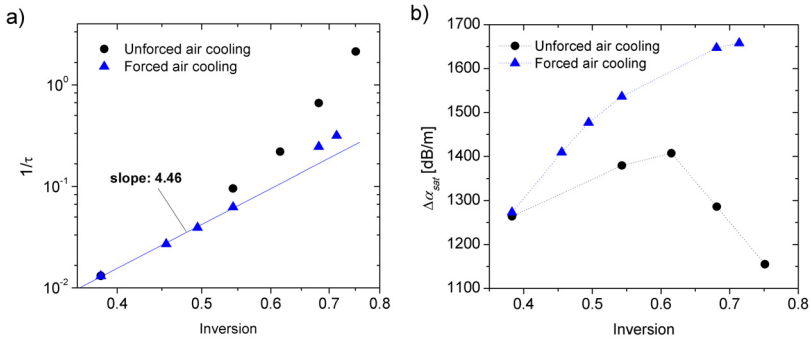

Figure 5.7: (a) Rate of photodarkening losses ($1/\tau$) as a function of inversion in logarithm scale. (b) Photodarkening saturation level $\Delta\alpha_{sat}$ versus inversion. (Publication IV)

For this reason, in publication IV a forced air cooling system was incorporated to the experimental setup in order to maintain the fiber temperature at low values, close to the RT. The fiber sample has no coating, which makes the heat removal more efficient. Figure 5.7(a) shows the $1/\tau$

derived from the stretched exponential fit to the photodarkening measurement as a function of the inversion, with both axes in logarithm scale. It can be observed that a straight line fits well to the lowest four inversion levels with a slope of $\sim$4.5. This result shows that the $1/\tau$ follows a simple power law relation with the inversion. This relation, known as the ion dependency, suggests that an average of 4 to 5 ions are involved in the process of creation of a color center. Two measurements at higher inversion levels appear off the initial trend, probably due to thermal related processes when using high pump powers, and, therefore, these measurements are not considered in the fitting.

In case the uncoated fiber sample is air cooled by natural convection, a forced linear curve fit to the measured data set results in a poor fitting with a slope of $\sim$7. This shows that the growth of the fiber thermal load with progressive photodarkening clearly disturbs the ion dependency measurement. In Fig. 5.7(b) the saturation loss level ($\Delta\alpha_{sat}$) is observed to have a linear increase with the inversion for the data set measured with forced air cooling and lower inversion levels. On the other hand, the $\Delta\alpha_{sat}$ measured with unforced air cooling shows an initial moderate increase with the inversion, which is reversed at the higher inversion levels.

The simple power law relation between $1/\tau$ and the inversion level was observed for the first time by Koponen et al. [91]. Since then, several ion dependency values ranging between 3.5 and 7 have been reported for different fibers [45, 91, 103, 104, 138]. In these studies, the fiber sample is commonly held in air or is immersed in water. Recoating of the sample is sometimes applied, which only exacerbates the heat load in the fiber core. Additionally, the probe wavelength is not carefully chosen to alleviate the effect of the spectral broadening with the fiber temperature. In Fig. 5.7(a), the ion dependency is reduced from 7 to 4.5 with a simple air cooling system and avoiding the use of high pump powers. This suggests that the discrepancy in the reported ion dependencies might be partly caused by an uncontrolled fiber temperature during the experiments, although other compositional or experimental differences cannot be ruled out.

Moreover, Jetschke et al. performed a detailed analysis of the fitting procedure that revealed a systematic error in determining the ion dependency [110]. If the decay curve was not saturated, the rate constant was found to be dependent on the measurement length. In a more recent publication by the same group, an ion dependency of 4.6 was observed, which

is in agreement with the result presented in Fig. 5.7 [138]. In that case, the fiber sample was immersed uncoated in pure water, which it is believed to be a more effective method of extracting heat from the fiber.

5.7 Isothermal measurements

The variations of the fiber temperature have a clear influence on the photodarkening evolution. If these temperature changes are not controlled, they introduce uncertainty in the measurement results, which are used to derive and analyze the photodarkening effect. Therefore, controlling the fiber core temperature at any conditions of pump power and photodarkening loss level is fundamental requirement to the progress in the characterization of photodarkening, and thus, in improving the understanding of the mechanisms driving the related color center formation.

Publication IV proposes a setup to control the fiber temperature based on a bath of a liquid metal alloy with high thermal conductivity. The choice for the liquid metal was Galinstan, which is an alloy of gallium, indium and tin in proportions typically of 68.5%, 21.5%, and 10%, respectively. Galinstan has a high thermal conductivity (about 30 times of water) and it enables experiments at low and high temperatures. A schematic of the isothermal bath is illustrated in Fig. 5.8. The melt container is made of high quality graphite, which is a material with about 5 times higher thermal conductivity than Galinstan alloy. The use of this container provides a good control of the fiber temperature, which is monitored by a protected thermocouple immersed in the liquid Galinstan bath. Furthermore, an array of linear halogen lamb tubes that are used for heating enables measurements at higher temperatures.

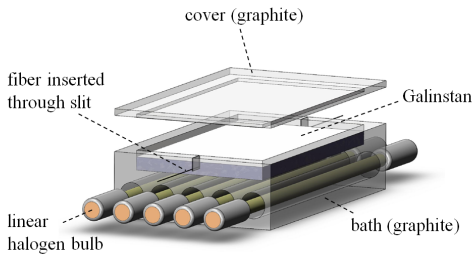

Figure 5.8: Schematics of the isothermal Galinstan bath. Dimensions are not to scale. (Publication IV)

The presented experimental setup was used to carry out photodarkening measurements at constant RT. In these experiments, the cladding pumping method was changed to core pumping (at 976 nm) to avoid losses of the pump power at the glass-Galinstan bath interface. The active fiber used was a single mode fiber with a core diameter of 6 μm and a total diameter of 125 μm. As it is typical in these experiments, the length of the active fiber was only 4 mm. Photodarkening was induced by a pump power of 200 mW.

To show the appropriateness of the method on controlling the fiber core temperature, the Galinstan bath was compared with three different methods of cooling: air cooling by natural convection (unforced air cooling), forced air cooling, and water bath. All the measurements, including the measurement with the Galinstan bath, were performed using the same undisturbed fiber sample. A summary of the photodarkening parameters derived from a stretched exponential fit to the measured curves is presented in Table 5.1. Since the fiber temperature was only monitored during the experiments with the Galinstan bath, a simulation model built in COMSOL Multiphysics version 4.2 was used to estimate the fiber core temperature at saturation of the losses in all the experiments, excluding forced air cooling.

Table 5.1: Photodarkening parameters derived from stretched exponential fit, and fiber core temperature determined by simulation.

Stretched exponential parameters	$\Delta\alpha_{sat}$ (dB/m)	τ (s)	β	R^2 (%)	Sim. temp. (°C)
Unforced air cooling	895.8	0.502	0.655	98.20	48.4
Forced air cooling	960.1	0.631	0.566	98.67	–
Water bath	957.4	0.673	0.583	98.73	26.0
Isothermal bath	961	0.688	0.584	98.64	24.7

Several observations were made from the results presented in Table 5.1. First, simulations show that the Galinstan bath is the most efficient cooling method, estimating a temperature change during the photodarkening experiment of less than 1 °C with respect to RT (24.2 °C). Second, the time constant was substantially different depending on the cooling method that was used, and the direction of change (i.e. lower values of the time constant) is consistent with an increase of the fiber temperature. This study

shows that a small temperature change of only 20 °C (owing to the use of unforced air cooling) can result in an increase of the rate parameter ($1/\tau$) by almost 40% in comparison to a measurement performed at the same pump power but using the isothermal bath.

This study illustrates the importance of maintaining the temperature constant during the experiments. It can also be concluded that the isothermal bath is an effective method of maintaining the fiber temperature constant at low and at elevated temperatures. Thereby, by eliminating the uncertainties in changing of the temperature, this method can be used to accurately determine the temperature dependence of photodarkening, and the ion dependence. Additionally, the isothermal bath approach can be especially useful when studying photo-bleaching processes due to the necessity of discriminating between thermal and photo-bleaching effects during the characterization.

6. Photodarkening- and thermal bleaching-induced refractive index change

The fiber core refractive index change (RIC) induced by photodarkening can be theoretically determined by the well-known Kramers-Krönig relations (KKR). However, an appropriate implementation of these relations requires an accurate measurement of the photodarkening spectrum, which is not straightforward given that instruments that cover a spectral range from NIR to deep into the UV are not commonly available. Additionally, the formation of color centers entails an atomic relaxation in the defect site taking place during the trapping of an electron or a hole [93]. This relaxation may imply an increase in the volume of the material, which may generate an additional RIC. Therefore, a direct measurement approach is much more preferable in studying the RIC induced by photodarkening, and also by thermal bleaching.

Calculations of the RIC based on the measurement of the photodarkening-induced loss spectrum indicated that the magnitude of the change expected is relatively small, Δn about $1{\cdot}10^{-5}$ at 1080 nm. Hence, interferometric methods have to be used to achieve sufficient resolution. Fotiadi et al. used a Mach-Zehnder fiber interferometer to quantify the RIC in single-mode Yb-doped fibers induced by population inversion [139]. In that case, an Yb-doped fiber sample of 2 m was included in one arm of the interferometer and it was core pumped at 980 nm (145 mW) with a short pulse of 2.5 ms. A rapid phase shift at the output signal of up to 4π rad was accurately detected at 1550 nm. However, photodarkening is a much slower effect and Mach-Zehnder fiber interferometers are not suitable for long-term measurements because they have separate interference arms with relatively long lengths, which make them susceptible to environmental perturbations, e.g., temperature variations and bending of the fiber, over a long period of time. Instead, in Publication V the photodarkening induced RIC was studied by using a simple and stable

modal interference method [140] that could be easily integrated in the photodarkening and thermal bleaching setup.

6.1 Measurement method

The modal interferometer was formed by splicing the Yb-doped fiber sample in the photodarkening setup with intentional core misalignment, as illustrated in Fig. 6.1. This method was proposed earlier in [140] and was used for measuring the RIC caused by UV irradiation [141].

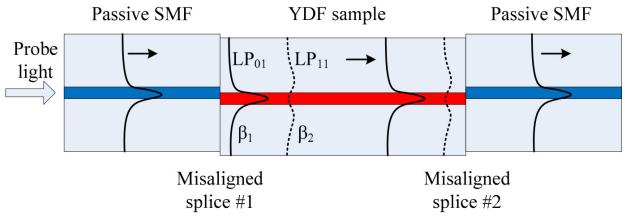

Figure 6.1: Misaligned splices for modal interference.

The power in the LP_{01} mode that propagates in the input fiber couples both to the LP_{01} and the LP_{11} mode at the first misalignment. The two modes then propagate in the active fiber with a different propagation constant, which leads to a phase mismatch. The interference then occurs at the second splice when a fraction of the power of the LP_{11} mode couples back to the LP_{01} mode of the output fiber. The stability of the interferometer is high as a consequence of the two modes sharing a short common interfering arm. This makes the method suitable for investigating the photodarkening induced RIC for a long duration. The fringe phase is given by $\phi = (\beta_1 - \beta_2)l$, where β_1 and β_2 are the propagation constants of LP_{01} and LP_{11} modes, respectively, and l is the length of the Yb-doped fiber sample. Photodarkening affects the doped core uniformly, generating a small RIC (Δn_{PD}), with respect to the fiber sample in pristine state. Thus, the modified propagation constants of the LP_{01} and the LP_{11} modes are given by [142]

$$\beta_i' = \beta_i + \frac{2\pi}{\lambda}\eta_i \Delta n_{PD}, (i = 1, 2) \tag{6.1}$$

where η_i (i = 1, 2) are the fractions of the power that propagate in the core as the LP_{01} and LP_{11} modes ($\eta_1 \sim 0.78$, and $\eta_1 \sim 0.1$ in the spectral

range near 1080 nm for the fibers used in the experiment). The relation of the photodarkening induced RIC with the phase shift of the interference fringe is given by [140]

$$\Delta n_{PD} = \frac{\lambda}{2\pi l\,(\eta_1 - \eta_2)}\Delta\phi. \tag{6.2}$$

6.2 Results

Figure 6.2(a) shows the oscillation of the fiber sample transmission as a function of the wavelength for the different levels of the photodarkening losses. The measurement of the spectrum is taken with the pump power off so that the influence of pump-induced RIC and the effect of temperature variation are avoided. The fringes shift towards longer wavelengths with increasing photodarkening loss, corresponding to positive RIC. Another important observation is that the shape of the curve is maintained well, and it proves the long-term stability of the interferometer. No relaxation of the phase shift was found for up to a few days indicating that the photodarkening-induced index change is permanent at room temperature. The phase shift $\Delta\phi$ can then be calculated from the wavelength difference T between the peaks/valleys and their shift ΔT using the relation $\Delta\phi = 2\pi\Delta T/T$. Using $\Delta\phi$ in Eq. (6.2) gives the RIC.

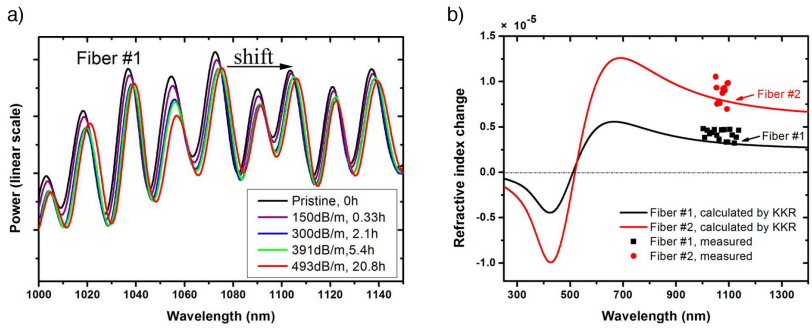

Figure 6.2: (a) Observed phase shift in the modal interference fringes at various photodarkening loss levels and corresponding times. (b) Scattered points: measured RIC by modal interference at the saturated photodarkening loss level. Lines: photodarkening-induced RIC as a function of wavelength, calculated by KKR. (Publication V)

This measurement method was employed to analyze two commercial fibers; Fiber #1 with a core diameter of 11.1 μm and Fiber #2 with a core diameter of 5.9 μm. The fiber samples were photodarkened up to

saturation of the losses and the RIC was measured at different wavelengths at the vicinity of 1080 nm. Figure 6.2.(b) shows the RIC as a function of the wavelength for both fiber samples at the level of saturation of the losses. The maximum Δn_{PD} of Fiber #1 and Fiber #2 was found to be $(0.42 \pm 0.055)\cdot 10^{-5}$ and $(0.88 \pm 0.10)\cdot 10^{-5}$, respectively. Solid lines plot the calculated RIC using the KKR based on the measurement of the absorption spectrum with a spectral range from 500 to 1400 nm and a Gaussian fit (performed in frequency) to estimate the spectrum at shorter wavelengths. The results are in fairly good agreement, although the RIC estimated with the KKR suggests values slightly smaller. This mismatch is attributed to an underestimation of the photodarkening loss level in the UV due to the Gaussian fit.

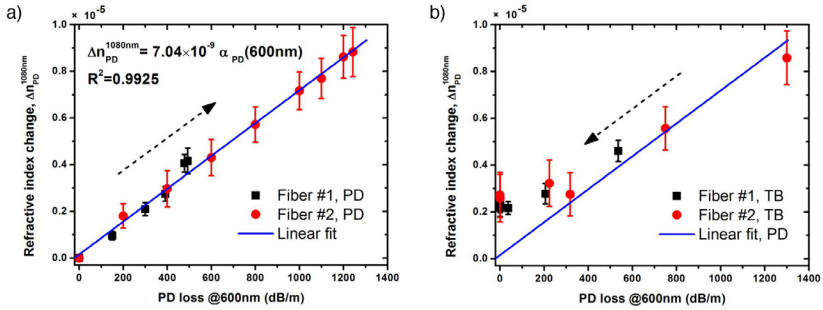

Figure 6.3: Measured RIC near 1080 nm versus photodarkening-induced loss at 600 nm: during photodarkening (a) and during thermal bleaching (b). (Publication V)

The evolution of the RIC with increasing photodarkening was also studied; see Fig. 6.3(a). For both fibers the RIC show a linear dependence with the photodarkening losses at 600 nm. This linear dependence is not limited to the probe wavelength, but it can also be extended to any arbitrary wavelength, since the photodarkening absorption spectrum preserves its shape at room temperature at any loss level. The evolution of Δn_{PD} at 1080 nm was also analyzed with decreasing photodarkening by thermal bleaching. At several different levels of remaining photodarkening loss, the fiber sample was cooled back down to room temperature to measure the phase shift interference. Figure 6.3(b) shows the RIC compared to the pristine state as a function of the photodarkening. A residual $\Delta n_{PD} \cong 0.2\cdot 10^{-5}$ remains for both fibers, although the photodarkening-induced loss in the spectral range of 500-1400 nm is completely recovered.

The reason for this nonbleachable RIC is not clear. The absorption spectrum of a thermally bleached sample was in the best case characterized

in a spectral range from 400 to 1400 nm. Therefore, the existence of non-bleached absorption peaks located deep in the UV band generated by another defect type cannot be ruled out. Upon using higher bleaching temperatures above 650 °C, e.g. 800 °C, a much higher RIC was observed, indicating that permanent structural changes in the host glass were created. Moreover, the repeatability study in section 4.3 indicated that photodarkening measurements are not affected by the thermal bleaching, suggesting that all the trapped charges are restored after thermal bleaching. A more probable possibility is that the residual RIC could be caused by a structural change in the host glass caused by the elevated temperature at 650 °C, in a similar way, but in a much lesser effect as it was observed when using 800 °C. In this case, it is interesting to observe that the magnitude of the residual RIC is similar for the two fiber samples, although the initial absolute levels of photodarkening losses were very different.

7. Fabrication of Yb-doped fibers with atomic layer deposition method

In Publication VI, a new all-vapor phase fabrication method for producing Yb-doped fibers was implemented. This method combines the well established modified chemical vapor deposition (MCVD) technique with atomic layer deposition (ALD). ALD enables coating of complex shapes and even porous structures with high aspect ratio. In this fabrication process, ALD was used to introduce the dopants in the porous soot material.

The next generation of LMA fiber lasers requires further improvement in terms of doping concentration, its uniformity, and accuracy in control of dopant and refractive index profiles while maintaining low background losses. The fabrication method presented in Publication VI can potentially result in an integrated ALD-MCVD system enabling accurate deposition/doping of tens of core layers that could allow the engineering of complex doping and refractive index profiles.

7.1 Fabrication process

The fabrication process of the ALD-MCVD preform entails three fabrication phases as described in Fig. 7.1. In the first phase, a porous SiO_2 is deposited inside a silica tube using a conventional MCVD-system (Nextrom OFC12). In this process, the gaseous $SiCl_4$ and O_2 are passed through the rotating silica tube and are heated by an external oxygen-hydrogen burner that traverses slowly along the rotating tube.

In the second phase, the MCVD-soot is transferred to a separate ALD equipment for doping with Yb_2O_3 and Al_2O_3. The soot-preform is positioned inside an in-house fabricated tube reactor for ensuring that the gas flow of precursors is well directed inside the soot-preform and that the purging of non-reacted chemicals is optimum. In this phase, the porous soot surface is coated with thin films of Yb_2O_3 and Al_2O_3.

Finally, in a third phase the soot-preform is transferred back to the MCVD-system, where the porous soot is, first, dried from adsorbed water and, second, sintered at a high temperature to form a transparent glass. After that, the soot-preform is collapsed into a solid rod and it is drawn into a fiber.

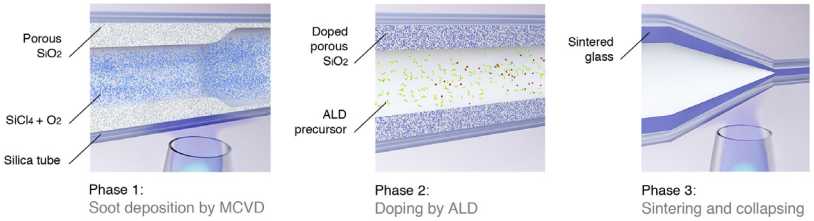

Figure 7.1: Phases of the fabrication process of an ALD-MCVD soot preform.

7.2 Doping by atomic layer deposition

The ALD process is a gas-phase vapor deposition process where the reactants are sequentially pulsed on the substrate surface to form a thin film of less than a monolayer thickness per one cycle [143, 144]. In ALD, the substrate is typically placed inside a chamber where it operates in vacuum. Before the ALD process starts, the soot-preform is stabilized to a given temperature. An ALD cycle can be divided into four steps:

Step 1. The first precursor (reactant A) is pulsed on the substrate to form a saturated layer by reacting with the soot surface.

Step 2. The continuous flow of nitrogen gas purges out the excess of precursor and reaction by-products.

Step 3. The soot surface is exposed to the second precursor (reactant B), which reacts with the first precursor as a self-terminating process.

Step 4. The excess precursor and reaction by-products are purged out by the nitrogen flow.

Figure 7.2 illustrates the steps of an ALD cycle. The gas reactants are pulsed separately into the chamber so that they do not get in contact in the gas phase. Therefore, the reaction can only occur on the surface. One reaction cycle deposits less than a monolayer thickness of material, which

allows precise thickness control. Nitrogen is used as a carrier of the precursors and as a purging gas between precursors pulses. The ytterbium and oxygen precursors used are β-diketonate $Yb(thd)_3$ and ozone O_3, respectively. Furthermore, the aluminum and oxygen precursors used are $Al(CH_3)_3$ and ozone O_3 [145].

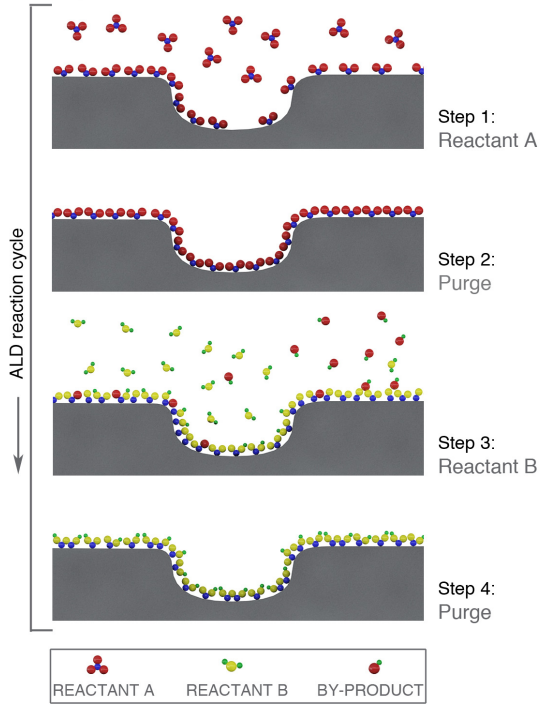

Figure 7.2: ALD reaction cycle steps. In Yb_2O_3 deposition, reactant A is $Yb(thd)_3$ and reactant B is O_3. In Al_2O_3 deposition, reactant A is $Al(CH_3)_3$ and reactant B is O_3.

The self-terminating aspect of the reaction enables coating of extremely high aspect ratio substrates such as the porous SiO_2 layer of the soot-preform [146]. In this case, the method of pulsing the precursors in steps 1 and 3 (see Fig. 7.2) is divided into two sub-steps (i.e., a micro-pulse and a micro-purge step) that are repeated hundreds of times. This approach is necessary to allow the penetration of the reactants at the pores located deep inside the substrate [Publication VI]. The distribution of the dopants in the porous soot layer was analyzed by an Scanning Electron Microscope (SEM) equipped with an Energy Dispersive Spectrometer (EDS) in the direction transversal to the soot preform length. The results revealed the ALD recipe reported in [Publication VI] was capable of doping the full depth of a 320 μm thick silica soot layer.

7.3 Fiber results

The presented manufacturing approach was used to fabricate a double cladding fiber with core and cladding dimensions of 18 μm and 125 μm, respectively, and a total length of 1 km. The resultant fiber had a core NA that varied from 0.07 to 0.08, and a background attenuation of about 20 dB/km at 1200 nm. Using the cut-back method, the Yb absorption was determined to be 107 dB/m at 920 nm, and showed an excellent uniformity along the 1km-long fiber, resulting in a maximum variation of 4% from its average value.

Moreover, the photodarkening propensity of the ALD-fiber was characterized as a function of the Al concentration, using the undesired decrease in the Al-concentration along the fiber. The distortion in the Al-doping was caused by small leakages of ambient air into the ozone line, and was fixed later [Publication VI]. Fiber samples of 2 cm length were cut out at different fiber positions and were cladding pumped with 10 W of pump power at 915 nm (inversion of 0.70) during 40 hours. Figure 7.3(a) shows the photodarkening losses after 40 hours of pumping in dB/m versus the Al concentration in atomic%. The plot can be fitted approximately by a linear curve, indicating that the concentration of defects can be reduced almost linearly in relation with the Al content. In a previous study, Jetschke et al. analyzed the photodarkening propensity on a series of fabricated fibers with a variable concentration of Al_2O_3 and a constant amount of Yb_2O_3 (about 0.45 mol%) and P_2O_5 (0.5 mol%) [128]. In this case, the photodarkening saturation loss level also decreased linearly with the Al content, clearly in line with the results in Fig. 7.3(a).

A comparison in terms of photodarkening between the MCVD-ALD fiber and a MCVD-solution doped fiber was performed. An MCVD-solution doped fiber with core and cladding diameters of 20 μm and 140 μm was prepared following the same MCVD recipe and same collapsing process that were used in the preparation of the ALD fiber. The fiber parameters and the measurement conditions are summarized in Table 7.1. A direct comparison of photodarkening propensity required adjusting the pump power to reach a similar density of the excited Yb ions ([Yb*]), i.e., the product of the density of Yb-ions and the population inversion, resulting in a very similar radial and longitudinal profile distribution. The results in Fig. 7.3(b) clearly show that the ALD-doped fiber suffers from less photodarkening in comparison to the fiber doped with solution doping. It

should also be noted that the Al/Yb concentrations ratio is lower in the ALD fiber (see Table 7.1). Therefore, the improved photodarkening resistance of the ALD-fiber compared to the solution doped-fiber is hypothesized to result as a consequence of a reduction in the Yb-ion clustering, due to the homogeneous Yb-ion incorporation by the ALD method before sintering and collapsing.

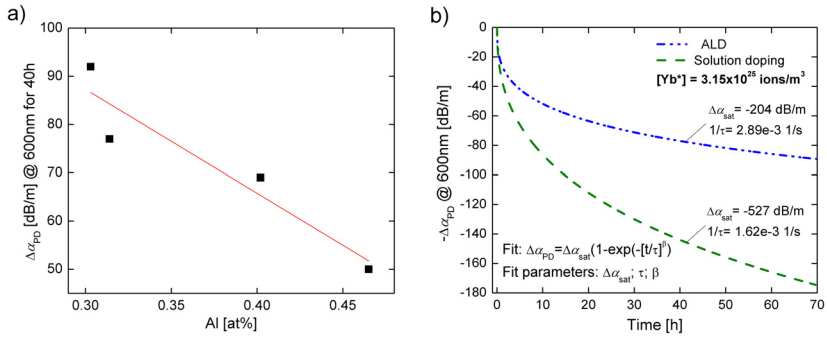

Figure 7.3: (a) The absorption coefficient change ($\Delta\alpha_{PD}$) at 600 nm after 40 hours of pumping is plotted versus the Al content expressed in atomic%. (b) Photodarkening benchmarking between an ALD-doped fiber and an MCVD-solution doping fiber with similar doping. [Yb*] is tuned to be approximately the same. Photodarkening measurements were fitted by a stretched exponential function. (Publication VI)

Table 7.1: Fiber parameters and measurement conditions of the photodarkening benchmarking

Fiber	Yb Conc. [atomic%]	Al Conc. [atomic%]	Al/Yb ratio	Inversion	[Yb*][a] ions/m^3	$\Delta\alpha_{PD}$ @ 70h[b] dB/m
ALD	0.07	0.31	4.4	0.72	3.15×10^{25}	90
Sol. doping	0.12	0.71	5.9	0.42	3.15×10^{25}	168

[a]Absolute number of the density of excited-state Yb^{3+} ions
[b]Photodarkening-induced loss after 70 hours of pumping

The different methods that have been used to reduce the effect of photodarkening are usually based on increasing the solubility of the Yb-ions in the host glass by adding co-dopants (see section 4.6). However, these methods have typically downside effects such us reduction of the Yb absorption and emission cross sections, increasing the fiber background attenuation or uncontrollably increasing the refractive index of the fiber. This highlights the importance of developing a method that increases the homogeneity of the doped material by means of improving the control and distribution homogeneity of the RE-ions. The ALD-doping method showed to have the potential to considerably promote diffusion of the RE-dopants and therefore reduce the formation of clusters.

In addition, the ALD fiber was tested in a fiber laser configuration. Measurements of the slope efficiency of a cladding-pumped fiber laser were used as a method to evaluate the laser efficiency of the fiber. A schematic of the fiber laser employed and the measured results are presented in the Fig. 7.4. A good slope efficiency of 80% was observed with the laser operating at 1080 nm and a pump wavelength of 915 nm.

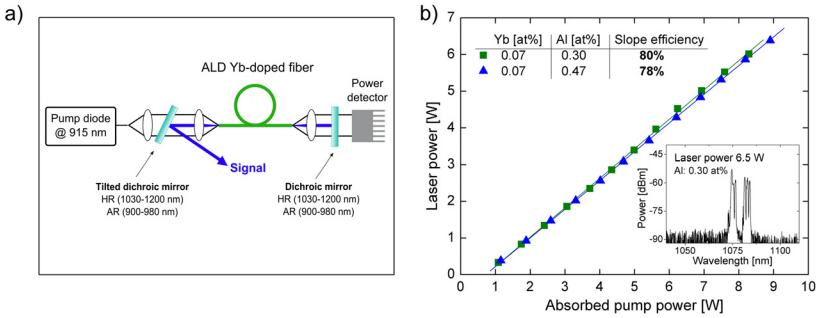

Figure 7.4: (a) Fiber laser configuration (b) Laser output power as a function of the absorbed pump power. Inset: laser spectrum for a laser output power of 6.5 W. (Publication VI)

7.4 Future work

The benefits in terms of reduction of Yb-ion clustering attributed to the ALD method in comparison to the standard solution doping method needs to be further studied. The direct relation between photodarkening and Yb clustering has been clearly shown [92]. However, a more direct method to determine the Yb-ions clustering (e.g. by measuring the cooperative luminescence [74, 76]) in a series of ALD and solution doped fibers with different dopant concentrations would be highly valuable and could confirm the results reported in [Publication VI].

The potential of the ALD method for soot doping encourages the development of a fabrication process that integrates ALD with the MCVD system. This system would allow several core layer deposition/doping cycles without the need to remove the preform from the MCVD system. This, in turn, would enable accurate in situ doping with significantly reduced fabrication time.

8. Summary and outlook

The main goal of this study was to measure photodarkening in Yb-doped silica fibers and to develop repeatable and accurate characterization methods to improve the understanding of the driving mechanism behind the photodarkening effect. An additional goal was to develop a novel fabrication method to produce advanced Yb-doped silica fibers with improved core material properties suitable for high power amplification.

A measurement method was developed to characterize both photodarkening and thermal bleaching [Publication IV]. This measurement method enables carrying out multiple measurements over the same sample, and thus eliminates uncertainties related to a change in the sample. A systematic study with several subsequent photodarkening measurements revealed only small differences in the derived parameters without any recognizable trend of drift, thus validating this approach.

In Publication II, the activation energy associated with the thermal recovery of photodarkening-induced losses was determined using the demarcation energy approach. The energy distribution of the photodarkening defects was found to be well described by a Gaussian-shape curve with a peak located at 1.32 eV and a FWHM of $\sim$0.31 eV. In this case, a complete recovery of the photodarkening losses occurred at energies $\geq$1.9 eV, which can be achieved with e.g. a fiber temperature of 600 °C for 47 s. However, thermal bleaching can also occur at much lower temperature, e.g. at 50 °C (although at much slower rate), which entails the necessity of performing the photodarkening measurements at temperatures close to the room temperature (or cooler) to avoid simultaneous recovery of defects that can complicate the interpretation of the data.

In Publication I, two new phenomena related to photodarkening were found, namely the post-irradiation heat-induced darkening and spectral broadening. Heat-induced darkening manifests as a net increase of loss

with increasing temperature prior to the initiation of thermal recovery. Similarities in the spectral shape of the induced losses indicated that the heat induced loss originates from the same type of defects that are created through pump irradiation. Additionally, the photodarkening-induced absorption spectrum was observed to exhibit a heat-induced spectral broadening, and the magnitude of the associated change in loss was shown to be proportional to $\mid \lambda - \lambda_0 \mid$ in the 550-850 nm spectral range, where λ_0 is the least temperature dependent wavelength (e.g. $\sim$600 nm for the fiber studied) [Publication I]. Furthermore, a measurement of the spectral broadening conducted at the pump wavelength (915 nm) in a photodarkened fiber was presented in Publication III. A noteworthy increase of loss was detected even at moderate temperatures. For the studied fiber, a photodarkened fiber operating at 100 °C exhibited an increase in the loss level of $>$50% with respect to the loss level at room temperature.

A method to quantify the fiber temperature during the course of photodarkening measurements was established in Publication III. The fiber temperature measured by a high resolution thermal camera was observed to increase with progressive photodarkening and reached up to 120 °C upon saturation of photodarkening. Furthermore, a model was implemented that took into account the combined effects of the Yb-silica quantum defect, the temperature dependence of the Yb-absorption cross section, and photodarkening-induced loss at 915 nm. This model accurately parameterized the temperature increase of a photodarkened fiber as a function of the pump power from room temperature to 120 °C. The observed thermal loading effect can progressively activate the effects of heat-induce darkening, spectral broadening and thermal bleaching during a photodarkening measurement, and consequently, exert a significant influence on photodarkening kinetics.

The relation of the inversion with the fiber temperature was analyzed using a simple model that takes into account the temperature dependence of the Yb-absorption cross section and the upper state lifetime [Publication IV]. The inversion in a fiber pumped with 10.5 W was found to deplete about 15% when the fiber temperature was increased from room temperature to 300 °C. The influence of the fiber temperature on the inversion is significant and should be considered when studying the thermal characteristics of the photodarkening parameters within a broad range of temperatures.

The aforementioned thermal effects illustrate the importance of accu-

rately controlling the fiber core temperature during photodarkening measurements [Publication IV]. A cooling method based on a forced air cooling system was employed to reduce the influence of temperature on the photodarkening measurement due to the absorbed pump power by photodarkening defects. By using this method, the photodarkening rate showed to follow a power law dependency of 4.5 on the inversion (ion dependence), suggesting that an average of 4 to 5 ions are involved in the process of creation of a color center. A more sophisticated setup based on a bath of a liquid metal alloy (Galinstan) was proposed to accurately control the fiber temperature, and based on simulations it was shown to be more efficient on extracting the thermal load compared to forced air cooling or using a water bath [Publication IV].

A modal interference method was used to measure and analyze the refractive index change induced by photodarkening and thermal bleaching in Yb-doped fibers [Publication V]. The photodarkening induced refractive index change was found to be positive and in the order of 10^{-5} at around 1080 nm in a sample photodarkened up to the saturation level. By using thermal bleaching, the increase of refractive index was partially erased, leaving a residual index change. The resulting increase of refractive index caused by photodarkening may induce mode distortion or phase retardation, which can be a concern in some applications. Moreover, it can also have an influence on the characteristics of fiber Bragg gratings inscribed in Yb-doped fibers.

Finally, in Publication VI, a new all-vapor phase fabrication method for producing Yb-doped fibers was implemented. This method combines the well established modified chemical vapor deposition (MCVD) technique with the ability of atomic layer deposition (ALD) to coat porous structures. A large mode area (LMA) Yb-doped aluminosilicate fiber was fabricated, showing uniform Yb-doping along the fiber axis, high lasing efficiency (with a characteristic slope efficiency of 80%), and low background losses. Moreover, photodarkening measurements showed less photodarkening propensity compared to a fiber with similar doping fabricated by the MCVD-solution doping technique with the same MCVD recipe. The versatility of the ALD method enables the development of a fabrication process that integrates ALD with the MCVD system allowing accurate in-situ doping with significantly reduced time compared to other methods such as solution doping.

Bibliography

[1] P. Becker, A. Olsson, and J. Simpson, *Erbium-doped fiber amplifiers: fundamentals and technology*. Academic press, 1999.

[2] G. BuAbbud, "High power fiber lasers and amplifiers for applications in telecommunications," in *Optical Fiber Communication (OFC), collocated National Fiber Optic Engineers Conference, 2010 Conference on (OFC/NFOEC)*, march 2010, p. 1.

[3] I. P. Corporation. [Online]. Available: http://www.ipgphotonics.com

[4] J. Hazey, V. Narula, D. Renton, K. Reavis, C. Paul, K. Hinshaw, P. Muscarella, E. Ellison, and W. Melvin, "Natural-orifice transgastric endoscopic peritoneoscopy in humans: initial clinical trial," *Surgical endoscopy*, vol. 22, no. 1, pp. 16–20, 2008.

[5] J. Kourambas, F. Delvecchio, and G. Preminger, "Low-power holmium laser for the management of urinary tract calculi, strictures, and tumors," *Journal of endourology*, vol. 15, no. 5, pp. 529–532, 2001.

[6] S. Jackson, "Towards high-power mid-infrared emission from a fibre laser," *Nature Photonics*, vol. 6, no. 7, pp. 423–431, 2012.

[7] E. Snitzer, "Proposed fiber cavities for optical masers," *Journal of Applied Physics*, vol. 32, no. 1, pp. 36–39, 1961.

[8] ——, "Optical maser action of Nd^{3+} in a barium crown glass," *Phys. Rev. Lett.*, vol. 7, pp. 444–446, Dec 1961.

[9] A. Schawlow and C. Townes, "Infrared and optical masers," *Physical Review*, vol. 112, no. 6, p. 1940, 1958.

[10] T. Maiman, "Stimulated optical radiation in ruby," 1960.

[11] C. Koester and E. Snitzer, "Amplification in a fiber laser," *Applied Optics*, vol. 3, no. 10, pp. 1182–1186, 1964.

[12] T. Miya, Y. Terunuma, T. Hosaka, and T. Miyashita, "Ultimate low-loss single-mode fibre at 1.55 μm," *Electronics Letters*, vol. 15, no. 4, pp. 106–108, 1979.

[13] S. Poole, D. Payne, and M. Fermann, "Fabrication of low-loss optical fibres containing rare-earth ions," *Electronics Letters*, vol. 21, no. 17, pp. 737–738, 1985.

[14] S. Poole, D. Payne, R. Mears, M. Fermann, and R. Laming, "Fabrication and characterization of low-loss optical fibers containing rare-earth ions," *Lightwave Technology, Journal of*, vol. 4, no. 7, pp. 870–876, 1986.

[15] J. Townsend, S. Poole, and D. Payne, "Solution-doping technique for fabrication of rare-earth-doped optical fibres," *Electronics letters*, vol. 23, no. 7, pp. 329–331, 1987.

[16] R. Mears, L. Reekie, I. Jauncey, and D. Payne, "Low-noise erbium-doped fibre amplifier operating at 1.54 μm," *Electronics Letters*, vol. 23, no. 19, pp. 1026–1028, 1987.

[17] E. Desurvire, J. Simpson, and P. Becker, "High-gain erbium-doped traveling-wave fiber amplifier," *Optics Letters*, vol. 12, no. 11, pp. 888–890, 1987.

[18] A. Tünnermann, T. Schreiber, F. Röser, A. Liem, S. Höfer, H. Zellmer, S. Nolte, and J. Limpert, "The renaissance and bright future of fibre lasers," *Journal of Physics B: Atomic, Molecular and Optical Physics*, vol. 38, no. 9, p. S681, 2005.

[19] Y. Jeong, J. Sahu, D. Payne, and J. Nilsson, "Ytterbium-doped large-core fiber laser with 1.36 kW continuous-wave output power," *Optics Express*, vol. 12, no. 25, pp. 6088–6092, 2004.

[20] D. Kliner, F. Di Teodoro, J. Koplow, S. Moore, and A. Smith, "Efficient second, third, fourth, and fifth harmonic generation of a Yb-doped fiber amplifier," *Optics communications*, vol. 210, no. 3, pp. 393–398, 2002.

[21] Y. Jeong, S. Yoo, C. Coderaard, J. Nilsson, J. Sahu, D. Payne, R. Horley, P. Turner, L. Hickey, A. Harker *et al.*, "Erbium: ytterbium codoped large-core fiber laser with 297-W continuous-wave output power," *Selected Topics in Quantum Electronics, IEEE Journal of*, vol. 13, no. 3, pp. 573–579, 2007.

[22] T. Ehrenreich, R. Leveille, I. Majid, K. Tankala, G. Rines, and P. Moulton, "1-kw, all-glass Tm: fiber laser," in *Proc. SPIE*, vol. 7580, 2010, pp. 7580–112.

[23] V. Fomin, M. Abramov, A. Ferin, A. Abramov, D. Mochalov, N. Platonov, and V. Gapontsev, "10 kW single-mode fiber laser," in *SyTu-1.3, Symposium on High-Power Fiber Lasers, 14th International Conference, Laser Optics*, 2010.

[24] D. Brown and H. Hoffman, "Thermal, stress, and thermo-optic effects in high average power double-clad silica fiber lasers," *Quantum Electronics, IEEE Journal of*, vol. 37, no. 2, pp. 207–217, 2001.

[25] D. Richardson, J. Nilsson, and W. Clarkson, "High power fiber lasers: current status and future perspectives [invited]," *JOSA B*, vol. 27, no. 11, pp. B63–B92, 2010.

[26] R. Paschotta, J. Nilsson, P. Barber, J. Caplen, A. Tropper, and D. Hanna, "Lifetime quenching in yb-doped fibres," *Optics Communications*, vol. 136, no. 5, pp. 375–378, 1997.

[27] J. J. Koponen, M. J. Söderlund, S. K. T. Tammela, and H. Po, "Photodarkening in ytterbium-doped silica fibers," pp. 599 008–599 008–10, 2005.

[28] E. Snitzer, H. Po, F. Hakimi, R. Tumminelli, and B. McCollum, "Double clad, offset core Nd fiber laser," in *Optical Fiber Sensors*. Optical Society of America, 1988.

[29] G. Agrawal, "Nonlinear fiber optics," *Nonlinear Science at the Dawn of the 21st Century*, pp. 195–211, 2000.

[30] D. DiGiovanni and A. Stentz, "Tapered fiber bundles for coupling light into and out of cladding-pumped fiber devices," Jan. 26 1999, uS Patent 5,864,644.

[31] R. Mears, L. Reekie, S. Poole, and D. Payne, "Neodymium-doped silica single-mode fibre lasers," *Electronics letters*, vol. 21, no. 17, pp. 738–740, 1985.

[32] D. Soh, S. Yoo, J. Nilsson, J. Sahu, K. Oh, S. Baek, Y. Jeong, C. Codemard, P. Dupriez, J. Kim *et al.*, "Neodymium-doped cladding-pumped aluminosilicate fiber laser tunable in the 0.9 μm wavelength range," *Quantum Electronics, IEEE Journal of*, vol. 40, no. 9, pp. 1275–1282, 2004.

[33] W. Koechner, *Solid-state laser engineering*. Springer, 2006, vol. 1.

[34] E. Snitzer, H. Po, F. Hakimi, R. Tumminelli *et al.*, "Erbium fiber laser amplifier at 1.55 μm with pump at 1.49 μm and Yb sensitized Er oscillator," in *Optical Fiber Communication Conference*. Optical Society of America, 1988.

[35] M. Nakazawa, Y. Kimura, and K. Suzuki, "Efficient Er^{3+}-doped optical fiber amplifier pumped by a 1.48 μm InGaAsP laser diode," *Applied Physics Letters*, vol. 54, no. 4, pp. 295–297, 1989.

[36] E. Snitzer and R. Woodcock, "Yb^{3+} - Er^{3+} glass laser," *Applied Physics Letters*, vol. 6, no. 3, pp. 45–46, 1965.

[37] J. Wu, Z. Yao, J. Zong, and S. Jiang, "Highly efficient high-power thulium-doped germanate glass fiber laser," *Optics letters*, vol. 32, no. 6, pp. 638–640, 2007.

[38] K. Lu and N. Dutta, "Spectroscopic properties of Yb-doped silica glass," *Journal of applied physics*, vol. 91, no. 2, pp. 576–581, 2002.

[39] H. Pask, R. Carman, D. Hanna, A. Tropper, C. Mackechnie, P. Barber, and J. Dawes, "Ytterbium-doped silica fiber lasers: versatile sources for the 1-1.2 μm region," *Selected Topics in Quantum Electronics, IEEE Journal of*, vol. 1, no. 1, pp. 2–13, 1995.

[40] E. Desurvire, *Erbium-doped fiber amplifiers: principles and applications*. Wiley New York, 1994, vol. 19.

[41] R. Paschotta, J. Nilsson, A. Tropper, and D. Hanna, "Ytterbium-doped fiber amplifiers," *Quantum Electronics, IEEE Journal of*, vol. 33, no. 7, pp. 1049–1056, 1997.

[42] C. Giles and E. Desurvire, "Modeling erbium-doped fiber amplifiers," *Lightwave Technology, Journal of*, vol. 9, no. 2, pp. 271–283, 1991.

[43] L. Zenteno, "High-power double-clad fiber lasers," *Lightwave Technology, Journal of*, vol. 11, no. 9, pp. 1435–1446, 1993.

[44] J. Koponen, M. Laurila, and M. Hotoleanu, "Inversion behavior in core-and cladding-pumped Yb-doped fiber photodarkening measurements," *Applied optics*, vol. 47, no. 25, pp. 4522–4528, 2008.

[45] J. Koponen, M. Söderlund, H. Hoffman, D. Kliner, J. Koplow, and M. Hotoleanu, "Photodarkening rate in Yb-doped silica fibers," *Applied optics*, vol. 47, no. 9, pp. 1247–1256, 2008.

[46] J. Limpert, F. Roser, S. Klingebiel, T. Schreiber, C. Wirth, T. Peschel, R. Eberhardt, and A. Tiinnermann, "The rising power of fiber lasers and amplifiers," *Selected Topics in Quantum Electronics, IEEE Journal of*, vol. 13, no. 3, pp. 537–545, 2007.

[47] V. Kovalev and R. Harrison, "Suppression of stimulated brillouin scattering in high-power single-frequency fiber amplifiers," *Optics letters*, vol. 31, no. 2, pp. 161–163, 2006.

[48] L. Zenteno, J. Wang, D. Walton, B. Ruffin, M. Li, S. Gray, A. Crowley, and X. Chen, "Suppression of Raman gain in single-transverse-mode dual-hole-assisted fiber," *Optics express*, vol. 13, no. 22, pp. 8921–8926, 2005.

[49] J. Kim, P. Dupriez, C. Codemard, J. Nilsson, and J. Sahu, "Suppression of stimulated Raman scattering in a high power Yb-doped fiber amplifier using a W-type core with fundamental mode cut-off," *Optics Express*, vol. 14, no. 12, pp. 5103–5113, 2006.

[50] T. Alkeskjold, "Large-mode-area ytterbium-doped fiber amplifier with distributed narrow spectral filtering and reduced bend sensitivity," *Optics Express*, vol. 17, no. 19, pp. 16 394–16 405, 2009.

[51] J. Kim, D. Shen, J. Sahu, and W. Clarkson, "Fiber-laser-pumped Er: YAG lasers," *Selected Topics in Quantum Electronics, IEEE Journal of*, vol. 15, no. 2, pp. 361–371, 2009.

[52] D. Taverner, D. Richardson, L. Dong, J. Caplen, K. Williams, and R. Penty, "158-μJ pulses from a single-transverse-mode, large-mode-area erbium-doped fiber amplifier," *Optics letters*, vol. 22, no. 6, pp. 378–380, 1997.

[53] D. Marcuse, "Field deformation and loss caused by curvature of optical fibers," *JOSA*, vol. 66, no. 4, pp. 311–320, 1976.

[54] J. Sakai and T. Kimura, "Bending loss of propagation modes in arbitrary-index profile optical fibers," *Applied Optics*, vol. 17, no. 10, pp. 1499–1506, 1978.

[55] J. Koplow, D. Kliner, and L. Goldberg, "Single-mode operation of a coiled multimode fiber amplifier," *Optics Letters*, vol. 25, no. 7, pp. 442–444, 2000.

[56] J. Sousa and O. Okhotnikov, "Multimode Er-doped fiber for single-transverse-mode amplification," *Applied physics letters*, vol. 74, no. 11, pp. 1528–1530, 1999.

[57] R. Farrow, G. Hadley, D. Kliner, and J. Koplow, "Design of refractive-index and rare-earth-dopant distributions for large-mode-area fibers used in coiled high-power amplifiers," in *Lasers and Applications in Science and Engineering*. International Society for Optics and Photonics, 2007, pp. 64 531C–64 531C.

[58] J. Marciante, "Gain filtering for single-spatial-mode operation of large-mode-area fiber amplifiers," *Selected Topics in Quantum Electronics, IEEE Journal of*, vol. 15, no. 1, pp. 30–36, 2009.

[59] C. Ye, J. Koponen, T. Kokki, J. Montiel i Ponsoda, A. Tervonen, and S. Honkanen, "Near-diffraction-limited output from confined-doped ytterbium fibre with 41 μm core diameter," *Electronics letters*, vol. 47, no. 14, pp. 819–821, 2011.

[60] M. Fermann, "Single-mode excitation of multimode fibers with ultrashort pulses," *Optics Letters*, vol. 23, no. 1, pp. 52–54, 1998.

[61] J. Alvarez-Chavez, A. Grudinin, J. Nilsson, P. Turner, and W. Clarkson, "Mode selection in high power cladding pumped fibre lasers with tapered section," in *Lasers and Electro-Optics, 1999. CLEO'99. Summaries of Papers Presented at the Conference on*. IEEE, 1999, pp. 247–248.

[62] A. Galvanauskas, M. Cheng, K. Hou, and K. Liao, "High peak power pulse amplification in large-core Yb-doped fiber amplifiers," *Selected Topics in Quantum Electronics, IEEE Journal of*, vol. 13, no. 3, pp. 559–566, 2007.

[63] J. Jasapara, M. Andrejco, A. DeSantolo, A. Yablon, Z. Vrallyay, J. Nicholson, J. Fini, D. DiGiovanni, C. Headley, E. Monberg *et al.*, "Diffraction-limited fundamental mode operation of core-pumped very-large-mode-area Er fiber amplifiers," *Selected Topics in Quantum Electronics, IEEE Journal of*, vol. 15, no. 1, pp. 3–11, 2009.

[64] L. Dong, J. Li, and X. Peng, "Bend-resistant fundamental mode operation in ytterbium-doped leakage channel fibers with effective areas up to 3160 μm^2," *Optics Express*, vol. 14, no. 24, pp. 11 512–11 519, 2006.

[65] J. Knight, T. Birks, P. Russell, and D. Atkin, "All-silica single-mode optical fiber with photonic crystal cladding," *Optics letters*, vol. 21, no. 19, pp. 1547–1549, 1996.

[66] T. Birks, J. Knight, and P. Russell, "Endlessly single-mode photonic crystal fiber," *Optics letters*, vol. 22, no. 13, pp. 961–963, 1997.

[67] P. Russell, "Photonic crystal fibers," *science*, vol. 299, no. 5605, pp. 358–362, 2003.

[68] C. Liu, G. Chang, N. Litchinister, D. Guertin, N. Jacobson, K. Tankala, and A. Galvanauskas, "Chirally coupled core fibers at 1550-nm and 1064-nm for effectively single-mode core size scaling," in *Conference on Lasers and Electro-Optics*. Optical Society of America, 2007.

[69] K. Arai, H. Namikawa, K. Kumata, T. Honda, Y. Ishii, and T. Handa, "Aluminum or phosphorus co-doping effects on the fluorescence and structural properties of neodymium-doped silica glass," *Journal of applied physics*, vol. 59, no. 10, pp. 3430–3436, 1986.

[70] G. Vienne, W. Brocklesby, R. Brown, Z. Chen, J. Minelly, J. Roman, and D. Payne, "Role of aluminum in ytterbium-erbium codoped phosphoaluminosilicate optical fibers," *Optical Fiber Technology*, vol. 2, no. 4, pp. 387–393, 1996.

[71] M. Shimizu, M. Yamada, M. Horiguchi, and E. Sugita, "Concentration effect on optical amplification characteristics of Er-doped silica single-mode fibers," *Photonics Technology Letters, IEEE*, vol. 2, no. 1, pp. 43–45, 1990.

[72] J. Kirchhof, S. Unger, S. Jetschke, A. Schwuchow, M. Leich, and V. Reichel, "Yb-doped silica-based laser fibers: correlation of photodarkening kinetics and related optical properties with the glass composition," in *Proc. of SPIE Vol*, vol. 7195, 2009, pp. 71 950S–1.

[73] S. Magne, Y. Ouerdane, M. Druetta, J. Goure, P. Ferdinand, and G. Monnom, "Cooperative luminescence in an ytterbium-doped silica fibre," *Optics communications*, vol. 111, no. 3, pp. 310–316, 1994.

[74] B. Schaudel, P. Goldner, M. Prassas, and F. Auzel, "Cooperative luminescence as a probe of clustering in yb^{3+} doped glasses," *Journal of alloys and compounds*, vol. 300, pp. 443–449, 2000.

[75] F. Auzel and P. Goldner, "Towards rare-earth clustering control in doped glasses," *Optical Materials*, vol. 16, no. 1, pp. 93–103, 2001.

[76] H. Gebavi, S. Taccheo, D. Milanese, A. Monteville, O. Le Goffic, D. Landais, D. Mechin, D. Tregoat, B. Cadier, and T. Robin, "Temporal evolution and correlation between cooperative luminescence and photodarkening in ytterbium doped silica fibers," *Optics Express*, vol. 19, no. 25, pp. 25 077–25 083, 2011.

[77] NEXTROM. [Online]. Available: http://www.nextrom.com

[78] J. Wang, D. Walton, and L. Zenteno, "All-glass high NA Yb-doped double-clad laser fibres made by outside-vapour deposition," *Electronics Letters*, vol. 40, no. 10, pp. 590–592, 2004.

[79] S. Sudo, M. Kawachi, T. Edahiro, T. Izawa, T. Shioda, and H. Gotoh, "Low-OH-content optical fibre fabricated by vapour-phase axial-deposition method," *Electronics Letters*, vol. 14, no. 17, pp. 534–535, 1978.

[80] S. Tammela, M. Soderlund, J. Koponen, V. Philippov, and P. Stenius, "The potential of direct nanoparticle deposition for the next generation of optical fibers," in *Proceedings of SPIE Photonics West*, vol. 6116, 2006, p. 16.

[81] J. Koponen, L. Petit, T. Kokki, V. Aallos, J. Paul, and H. Ihalainen, "Progress in direct nanoparticle deposition for the development of the next generation fiber lasers," *Optical Engineering*, vol. 50, no. 11, pp. 111 605–111 605, 2011.

[82] B. Ainslie, "A review of the fabrication and properties of erbium-doped fibers for optical amplifiers," *Lightwave Technology, Journal of*, vol. 9, no. 2, pp. 220–227, 1991.

[83] R. Tumminelli, B. McCollum, and E. Snitzer, "Fabrication of high-concentration rare-earth doped optical fibers using chelates," *Lightwave Technology, Journal of*, vol. 8, no. 11, pp. 1680–1683, 1990.

[84] A. Webb, A. Boyland, R. Standish, S. Yoo, J. Sahu, and D. Payne, "MCVD in-situ solution doping process for the fabrication of complex design large core rare-earth doped fibers," *Journal of Non-Crystalline Solids*, vol. 356, no. 18, pp. 848–851, 2010.

[85] S. Tammela, M. Hotoleanu, P. Kiiveri, H. Valkonen, S. Sarkilahti, and K. Janka, "Very short Er-doped silica glass fiber for L-band amplifiers," in *Optical Fiber Communications Conference, 2003. OFC 2003*. IEEE, 2003, pp. 376–377.

[86] M. Cheng, K. Hou, A. Galvanauskas, D. Engin, R. Changkakoti, and P. Mamidipudi, "High average power generation of single-transverse mode MW-peak power pulses using 80-μm core Yb-doped LMA fibers," in *Lasers and Electro-Optics, 2006 and 2006 Quantum Electronics and Laser Science Conference. CLEO/QELS 2006. Conference on*. IEEE, 2006, pp. 1–2.

[87] A. Boyland, A. Webb, M. Kalita, S. Yoo, C. Codemard, R. Standish, J. Nilsson, and J. Sahu, "Rare earth doped optical fiber fabrication using novel gas phase deposition technique," in *Conference on Lasers and Electro-Optics*. Optical Society of America, 2010.

[88] A. Boyland, A. Webb, S. Yoo, F. Mountfort, M. Kalita, R. Standish, J. Sahu, D. Richardson, and D. Payne, "Optical fiber fabrication using novel gas-phase deposition technique," *Journal of Lightwave Technology*, vol. 29, no. 6, pp. 912–915, 2011.

[89] E. Sekiya, P. Barua, K. Saito, and A. Ikushima, "Fabrication of Yb-doped silica glass through the modification of MCVD process," *Journal of Non-Crystalline Solids*, vol. 354, no. 42, pp. 4737–4742, 2008.

[90] J. Koponen, M. Söderlund, H. Hoffman, and S. Tammela, "Measuring photodarkening from single-mode ytterbium doped silica fibers," *Opt. Express*, vol. 14, no. 24, pp. 11 539–11 544, 2006.

[91] J. Koponen, M. Söderlund, H. Hoffman, D. Kliner, and J. Koplow, "Photodarkening measurements in large mode area fibers," in *Lasers and Applications in Science and Engineering*. International Society for Optics and Photonics, 2007, pp. 64 531E–64 531E.

[92] B. Morasse, S. Chatigny, É. Gagnon, C. Hovington, J. Martin, and J. de Sandro, "Low photodarkening single cladding ytterbium fibre amplifier," in *Lasers and Applications in Science and Engineering*. International Society for Optics and Photonics, 2007, pp. 64 530H–64 530H.

[93] L. Glebov, "Linear and nonlinear photoionization of silicate glasses," *GLASS SCIENCE AND TECHNOLOGY-FRANKFURT AM MAIN-*, vol. 75, pp. 1–6, 2004.

[94] M. Engholm and L. Norin, "Preventing photodarkening in ytterbium-doped high power fiber lasers; correlation to the UV-transparency of the core glass," *Optics express*, vol. 16, no. 2, pp. 1260–1268, 2008.

[95] S. Yoo, C. Basu, A. Boyland, C. Sones, J. Nilsson, J. Sahu, and D. Payne, "Photodarkening in Yb-doped aluminosilicate fibers induced by 488 nm irradiation," *Optics letters*, vol. 32, no. 12, pp. 1626–1628, 2007.

[96] K. Mattsson, S. Knudsen, B. Cadier, and T. Robin, "Photo darkening in ytterbium co-doped silica material," in *Proceedings of SPIE*, vol. 6873, 2008, p. 68731C.

[97] M. Broer, D. Krol, and D. DiGiovanni, "Highly nonlinear near-resonant photodarkening in a thulium-doped aluminosilicate glass fiber," *Optics letters*, vol. 18, no. 10, pp. 799–801, 1993.

[98] M. Broer, R. Cone, and J. Simpson, "Ultraviolet-induced distributed-feedback gratings in Ce^{3+}-doped silica optical fibers," *Optics letters*, vol. 16, no. 18, pp. 1391–1393, 1991.

[99] G. Atkins and A. Carter, "Photodarkening in Tb^{3+}-doped phosphosilicate and germanosilicate optical fibers," *Optics letters*, vol. 19, no. 12, pp. 874–876, 1994.

[100] E. Behrens, R. Powell, and D. Blackburn, "Characteristics of laser-induced gratings in Pr^{3+}-and Eu^{3+}-doped silicate glasses," *JOSA B*, vol. 7, no. 8, pp. 1437–1444, 1990.

[101] G. Atkins and F. Ouellette, "Reversible photodarkening and bleaching in Tb^{3+}-doped optical fibers," *Optics letters*, vol. 19, no. 13, pp. 951–953, 1994.

[102] T. Kitabayashi, M. Ikeda, M. Nakai, T. Sakai, K. Himeno, and K. Ohashi, "Population inversion factor dependence of photodarkening of Yb-doped fibers and its suppression by highly aluminum doping," in *Optical Fiber Communication Conference and Exposition and The National Fiber Optic Engineers Conference*. Optical Society of America, 2006, p. OThC5.

[103] A. Shubin, M. Yashkov, M. Melkumov, S. Smirnov, I. Bufetov, and E. Dianov, "Photodarkening of alumosilicate and phosphosilicate Yb-doped fibers," in *Lasers and Electro-Optics, 2007 and the International Quantum Electronics Conference. CLEOE-IQEC 2007. European Conference on*. IEEE, 2007, pp. 1–1.

[104] S. Jetschke, S. Unger, U. Röpke, and J. Kirchhof, "Photodarkening in Yb doped fibers: experimental evidence of equilibrium states depending on the pump power," *Optics express*, vol. 15, no. 22, pp. 14 838–14 843, 2007.

[105] J. Jasapara, M. Andrejco, D. DiGiovanni, and R. Windeler, "Effect of heat and H_2 gas on the photo-darkening of Yb^{+3} fibers," in *Conference on Lasers and Electro-Optics*. Optical Society of America, 2006.

[106] I. Manek-Hönninger, J. Boullet, T. Cardinal, F. Guillen, S. Ermeneux, M. Podgorski, R. Bello Doua, and F. Salin, "Photodarkening and photobleaching of an ytterbium-doped silica double-clad LMA fiber," *Optics express*, vol. 15, no. 4, pp. 1606–1611, 2007.

[107] A. Guzman Chávez, A. Kir'yanov, Y. Barmenkov, and N. Il'Ichev, "Reversible photo-darkening and resonant photobleaching of Ytterbium-doped silica fiber at in-core 977-nm and 543-nm irradiation," *Laser Physics Letters*, vol. 4, no. 10, pp. 734–739, 2007.

[108] H. Gebavi, S. Taccheo, D. Tregoat, A. Monteville, and T. Robin, "Photobleaching of photodarkening in ytterbium doped aluminosilicate fibers with 633 nm irradiation," *Opt. Mater. Express*, vol. 2, no. 9, pp. 1286–1291, Sep 2012.

[109] J. Montiel i Ponsoda, M. Söderlund, J. Koplow, J. Koponen, A. Iho, and S. Honkanen, "Combined photodarkening and thermal bleaching measurement of an ytterbium-doped fiber," in *SPIE LASE: Lasers and Applications*

in Science and Engineering. International Society for Optics and Photonics, 2009, pp. 71 952D–71 952D.

[110] S. Jetschke and U. Röpke, "Power-law dependence of the photodarkening rate constant on the inversion in Yb doped fibers," *Optics letters*, vol. 34, no. 1, pp. 109–111, 2009.

[111] M. Engholm, L. Norin, and D. Åberg, "Strong UV absorption and visible luminescence in ytterbium-doped aluminosilicate glass under UV excitation," *Optics letters*, vol. 32, no. 22, pp. 3352–3354, 2007.

[112] M. Söderlund, J. Montiel i Ponsoda, and S. Honkanen, "Measurement of thermal binding energy of photodarkening-induced color centers in ytterbium-doped silica fibers," in *Lasers and Electro-Optics 2009 and the European Quantum Electronics Conference. CLEO Europe-EQEC 2009. European Conference on*. IEEE, 2009, pp. 1–1.

[113] T. Erdogan, V. Mizrahi, P. J. Lemaire, and D. Monroe, "Decay of ultraviolet-induced fiber Bragg gratings," *Journal of Applied Physics*, vol. 76, no. 1, pp. 73 –80, jul 1994.

[114] S. Kannan, M. LuValle, R. Ahrens, and P. Lemaire, "Analysis of recovery in radiation-induced loss in rare-earth-doped fibers through master curve/demarcation energy diagrams," in *Optical Fiber Communication Conference, 1999, and the International Conference on Integrated Optics and Optical Fiber Communication. OFC/IOOC'99. Technical Digest*, vol. 3. IEEE, 1999, pp. 93–95.

[115] Y. Lee, S. Sinha, M. Digonnet, R. Byer, and S. Jiang, "Measurement of high photodarkening resistance in heavily Yb^{3+}-doped phosphate fibres," *Electronics letters*, vol. 44, no. 1, pp. 14–16, 2008.

[116] M. Engholm and L. Norin, "Comment on "photodarkening in Yb-doped aluminosilicate fibers induced by 488 nm irradiation"," *Optics letters*, vol. 33, no. 11, pp. 1216–1216, 2008.

[117] S. Yoo, C. Basu, A. Boyland, C. Sones, J. Nilsson, J. Sahu, and D. Payne, "Reply to comment on "photodarkening in Yb-doped aluminosilicate fibers induced by 488 nm irradiation"," *Optics Letters*, vol. 33, no. 11, pp. 1217–1218, 2008.

[118] A. Rybaltovsky, S. Aleshkina, M. Likhachev, M. Bubnov, A. Umnikov, M. Yashkov, A. Gur'yanov, and E. Dianov, "Luminescence and photoinduced absorption in ytterbium-doped optical fibres," *Quantum Electronics*, vol. 41, no. 12, pp. 1073–1079, 2011.

[119] F. Mady, M. Benabdesselam, and W. Blanc, "Thermoluminescence characterization of traps involved in the photodarkening of ytterbium-doped silica fibers," *Optics letters*, vol. 35, no. 21, pp. 3541–3543, 2010.

[120] P. Dragic, C. Carlson, and A. Croteau, "Characterization of defect luminescence in yb doped silica fibers: part I NBOHC," *Optics Express*, vol. 16, no. 7, pp. 4688–4697, 2008.

[121] P. Dragic, Y. Liu, T. Galvin, and J. Eden, "Ultraviolet absorption and excitation spectroscopy of rare-earth-doped glass fibers derived from glassy and crystalline preforms," in *Proceedings of SPIE*, vol. 8237, 2012, p. 82370T.

[122] T. Arai, K. Ichii, S. Tanigawa, and M. Fujimaki, "Defect analysis of photodarkened and gamma-ray irradiated ytterbium-doped silica glasses," in *Optical Fiber Communication Conference*. Optical Society of America, 2009.

[123] R. Peretti, A. Jurdyc, B. Jacquier, C. Gonnet, A. Pastouret, E. Burov, and O. Cavani, "How do traces of thulium explain photodarkening in Yb doped fibers?" *Optics Express*, vol. 18, no. 19, pp. 20 455–20 460, 2010.

[124] R. Peretti, C. Gonnet, and A. Jurdyc, "Revisiting literature observations on photodarkening in Yb^{3+} doped fiber considering the possible presence of Tm impurities," *Journal of Applied Physics*, vol. 112, no. 9, pp. 093 511–093 511, 2012.

[125] S. Jetschke, M. Leich, S. Unger, A. Schwuchow, and J. Kirchhof, "Influence of Tm-or Er-codoping on the photodarkening kinetics in Yb fibers," *Optics Express*, vol. 19, no. 15, pp. 14 473–14 478, 2011.

[126] J. Dawson, M. Messerly, R. Beach, M. Shverdin, E. Stappaerts, A. Sridharan, P. Pax, J. Heebner, C. Siders, and C. Barty, "Analysis of the scalability of diffraction-limited fiber lasers and amplifiers to high average power," *Optics express*, vol. 16, no. 17, pp. 13 240–13 266, 2008.

[127] S. Unger, A. Schwuchow, S. Jetschke, V. Reichel, A. Scheffel, and J. Kirchhof, "Optical properties of Yb-doped laser fibers in dependence on codopants and preparation conditions," in *Proc. SPIE*, vol. 6890, 2008, pp. 689 016–1.

[128] S. Jetschke, S. Unger, A. Schwuchow, M. Leich, and J. Kirchhof, "Efficient Yb laser fibers with low photodarkening by optimization of the core composition," *Optics express*, vol. 16, no. 20, pp. 15 540–15 545, 2008.

[129] M. Engholm, P. Jelger, F. Laurell, and L. Norin, "Improved photodarkening resistivity in ytterbium-doped fiber lasers by cerium codoping," *Optics letters*, vol. 34, no. 8, pp. 1285–1287, 2009.

[130] M. Leich, S. Jetschke, S. Unger, and J. Kirchhof, "Temperature influence on the photodarkening kinetics in Yb-doped silica fibers," *JOSA B*, vol. 28, no. 1, pp. 65–68, 2011.

[131] S. Yoo, A. Boyland, R. Standish, and J. Sahu, "Measurement of photodarkening in Yb-doped aluminosilicate fibres at elevated temperature," *Electronics letters*, vol. 46, no. 3, pp. 243–244, 2010.

[132] J. Sahu, S. Yoo, A. Boyland, C. Basu, M. Kalita, A. Webb, C. Sones, J. Nilsson, and D. Payne, "488 nm irradiation induced photodarkening study of Yb-doped aluminosilicate and phosphosilicate fibers," in *Quantum Electronics and Laser Science Conference*. Optical Society of America, 2008.

[133] C. Basu, S. Yoo, A. Boyland, A. Webb, C. Sones, and J. Sahu, "Influence of temperature on the post-irradiation temporal loss evolution in Yb-doped aluminosilicate fibers, photodarkened by 488 nm CW irradiation," in *The European Conference on Lasers and Electro-Optics*. Optical Society of America, 2009.

[134] M. Leich, U. Röpke, S. Jetschke, S. Unger, V. Reichel, and J. Kirchhof, "Non-isothermal bleaching of photodarkened Yb-doped fibers," *Optics express*, vol. 17, no. 15, pp. 12 588–12 593, 2009.

[135] D. Grukh, A. Kurkov, V. Paramonov, and E. Dianov, "Effect of heating on the optical properties of Yb^{3+}-doped fibres and fibre lasers," *Quantum Electronics*, vol. 34, no. 6, pp. 579–582, 2004.

[136] Y. Wang, C. Xu, and H. Po, "Thermal effects in kilowatt fiber lasers," *Photonics Technology Letters, IEEE*, vol. 16, no. 1, pp. 63–65, 2004.

[137] T. Newell, P. Peterson, A. Gavrielides, and M. Sharma, "Temperature effects on the emission properties of Yb-doped optical fibers," *Optics communications*, vol. 273, no. 1, pp. 256–259, 2007.

[138] S. Jetschke, U. Röpke, S. Unger, and J. Kirchhof, "Characterization of photodarkening processes in Yb doped fibers," in *Proc. SPIE*, vol. 7195, 2009, p. 71952B.

[139] A. Fotiadi, O. Antipov, and P. Mugret, "Dynamics of pump-induced refractive index changes in single-mode Yb-doped optical fibers," *Optics Express*, vol. 16, no. 17, pp. 12 658–12 663, 2008.

[140] J. Canning and A. Carter, "Modal interferometer for in situ measurements of induced core index change in optical fibers," *Optics letters*, vol. 22, no. 8, pp. 561–563, 1997.

[141] J. Canning, A. Carter, and M. Sceats, "Correlation between photodarkening and index change during 193 nm irradiation of germanosilicate and phosphosilicate fibers," *Lightwave Technology, Journal of*, vol. 15, no. 8, pp. 1348–1356, 1997.

[142] A. Snyder and J. Love, *Optical waveguide theory*. Springer, 1983, vol. 190.

[143] R. Puurunen, "Surface chemistry of atomic layer deposition: A case study for the trimethylaluminum/water process," *Journal of applied physics*, vol. 97, no. 12, pp. 121 301–121 301, 2005.

[144] S. George, "Atomic layer deposition: An overview," *Chem. Rev.*, vol. 110, no. 1, pp. 111–131, 2010.

[145] J. Kim, K. Chakrabarti, J. Lee, K. Oh, and C. Lee, "Effects of ozone as an oxygen source on the properties of the Al_2O_3 thin films prepared by atomic layer deposition," *Materials chemistry and physics*, vol. 78, no. 3, pp. 733–738, 2003.

[146] J. Elam, D. Routkevitch, P. Mardilovich, and S. George, "Conformal coating on ultrahigh-aspect-ratio nanopores of anodic alumina by atomic layer deposition," *Chemistry of Materials*, vol. 15, no. 18, pp. 3507–3517, 2003.

Fiber lasers and amplifiers have become very important for many applications, such as telecommunications, materials processing, and medicine. Ytterbium (Yb) doped fibers are the preferred gain media in high peak and average power laser sources. However, the photodarkening effect, which manifests as a time dependent increase of loss in the doped core, is one of the main threats to the efficiency of the Yb-doped gain media leading to degradation of the laser performance. This thesis focused on developing accurate methods to characterize photodarkening and the associated thermal effects in Yb-doped silica fibers. Parallel to the experimental work on photodarkening, a new all vapor phase fabrication method was implemented to produce Yb-doped fibers by atomic layer deposition (ALD) in combination with the conventional modified chemical vapor deposition (MCVD) technique.

Aalto-DD 101/2013

ISBN 978-952-60-5216-8
ISBN 978-952-60-5217-5 (pdf)
ISSN-L 1799-4934
ISSN 1799-4934
ISSN 1799-4942 (pdf)

Aalto University
School of Electrical Engineering
Department of Micro- and Nanosciences
www.aalto.fi